nature methods

Article

https://doi.org/10.1038/s41592-024-02583-1

A deep learning pipeline for three-dimensional brain-wide mapping of local neuronal ensembles in teravoxel light-sheet microscopy

Received: 22 December 2023

Accepted: 26 November 2024

Published online: 27 January 2025

Check for updates

Ahmadreza Attarpour[1,2,3], Jonas Osmann[2,3], Anthony Rinaldi[2,3], Tianbo Qi[4,5], Neeraj Lal[4,5], Shruti Patel[2,3], Matthew Rozak[1,2,3], Fengqing Yu[2,3], Newton Cho[6,7], Jordan Squair[6,7,8], JoAnne McLaurin[9,10], Misha Raffiee[11,12], Karl Deisseroth[11,12], Gregoire Courtine[6,7,8], Li Ye[4,5], Bojana Stefanovic[1,2,3,14] & Maged Goubran[1,2,3,13,14] ✉

Teravoxel-scale, cellular-resolution images of cleared rodent brains acquired with light-sheet fluorescence microscopy have transformed the way we study the brain. Realizing the potential of this technology requires computational pipelines that generalize across experimental protocols and map neuronal activity at the laminar and subpopulation-specific levels, beyond atlas-defined regions. Here, we present artificial intelligence-based cartography of ensembles (ACE), an end-to-end pipeline that employs three-dimensional deep learning segmentation models and advanced cluster-wise statistical algorithms, to enable unbiased mapping of local neuronal activity and connectivity. Validation against state-of-the-art segmentation and detection methods on unseen datasets demonstrated ACE's high generalizability and performance. Applying ACE in two distinct neurobiological contexts, we discovered subregional effects missed by existing atlas-based analyses and showcase ACE's ability to reveal localized or laminar neuronal activity brain-wide. Our open-source pipeline enables whole-brain mapping of neuronal ensembles at a high level of precision across a wide range of neuroscientific applications.

Mapping neuronal activity and morphology is critical for understanding brain network dynamics underlying behavior and cognition[1,2]. Advances in microscopy, such as light-sheet fluorescence microscopy (LSFM)[3,4], and tissue-clearing techniques, such as CLARITY[5], CUBIC[6], iDISCO[7] and SHIELD[8,9], have enabled high-fidelity imaging of cellular structures in intact tissue, providing insights into brain structure and function. However, these state-of-the-art imaging and molecular methods produce exceedingly large (teravoxel scale with trillions of voxels), complex, multichannel and three-dimensional (3D) datasets. Such teravoxel-scale datasets require automated algorithms for analyses and identification of focal brain-wide changes in neuroanatomy or neurophysiology[2,10,11].

To enable automated brain-wide activity mapping in large microscopy datasets, current pipelines (such as ClearMap[1] and multimodal image registration and connectivity analysis (MIRACL)[10]) rely on registration to standardized brain atlases or common reference spaces for statistical analyses, via a region-of-interest (ROI)-based approach[2,12]. This analysis requires a priori knowledge or data-specific

A full list of affiliations appears at the end of the paper. ✉e-mail: maged.goubran@utoronto.ca

expertise in choosing regions of interest according to the designed experiments and comparison of cell counts across groups[1,2] (due to the large number of brain regions). Notwithstanding, emerging single-cell and spatial-omics data indicate far greater diversity within conventionally defined atlas regions, with neuronal subpopulations having unique cytoarchitecture, connectivity and function[13]. Moreover, definitions of atlas regions are commonly structure-centric and limited in regard to delineation of neuronal subtypes. Reliance on a traditional, region-based grouping of voxels can thus fail to detect subtle focal contrasts or neuronal subpopulation-specific effects in an unbiased fashion. Further, aggregating results on a regional basis obscures the heterogeneity of changes within brain regions; nevertheless, many pathologies are thought to exert salient laminar or columnar effects[14–18]. In addition to regional analyses, existing pipelines for LSFM data enable voxel-wise statistical analyses to assess neuronal changes in different brain regions. However, in vivo neuroimaging studies have demonstrated that voxel-wise statistical tests with leniently corrected *P* values can result in an inflated rate of false positives (FP)[19], and this issue is amplified with teravoxel-scale LSFM images. Conversely, conservative corrections such as Benjamini and Hochberg[20] reduce the power of these voxel-wise methods to detect salient changes in such teravoxel datasets.

Pipelines commonly employed for cellular segmentation using fluorescent microscopy images, such as ClearMap[1], WholeBrain[21] and Ilastik[22], rely on traditional image-processing techniques in which parameter tuning or expert intervention is often required to extract meaningful features for segmentation[23]. This limits their ability to produce robust results on unseen datasets, with varying signal and noise distribution across different experimental set-ups and brain regions[24]. Deep learning (DL) models can automatically learn effective representations of data with multiple levels of abstraction, resulting in accurate and robust segmentation of imaging data[25,26]. Although several pipelines have been introduced to leverage DL for mapping of cells in microscopy data, none of the available DL pipelines are specifically tailored for 3D mapping of neuronal activity in whole-brain LSFM data. Current DL pipelines are confounded by any the following: (1) reliance on two-dimensional (2D)-based models, such as Cellpose[27,28] and STARDIST[29], which impedes the unbiased assessment of 3D volumetric changes; (2) training and testing on restricted datasets consisting of a small sample from specific brain regions and cell types, such as CDeep3M[30] and DeLTA[31], limiting their ability to generalize or segment a large variety of cell sizes, shapes and densities[32]; and (3) combining conventional image-processing techniques with a DL-based classifier, such as Cellfinder[33], limiting their functionality to detection. Furthermore, current segmentation pipelines do not provide uncertainty estimates of model predictions, which are invaluable for evaluating the reliability of segmentation models, and for guiding the improvement of segmentation results[34].

To address these critical opportunities and enable robust brain-wide mapping of neural subpopulation-specific effects in LSFM data, we developed the ACE pipeline. This end-to-end, automated pipeline utilizes cutting-edge DL segmentation models and advanced statistical algorithms, enabling unbiased 3D mapping of neuronal activity and morphometrical changes in teravoxel-scale LSFM data. Unlike existing methods, ACE, via integration with our MIRAC[10] open-source platform, provides a quantitative mapping of neuronal subtype-specific effects in an atlas-agnostic manner that is independent of predefined atlas regions. Our threshold-free, cluster-wise permutation analysis (optimized for LSFM data) enables cluster-based statistical analysis and improves the sensitivity of voxel-wise analysis. Leveraging DL segmentation maps and atlas registration, clusters detected at the atlas space are further validated at the native space of each subject. We trained ACE segmentation models on large LSFM datasets and validated them against the most commonly used state-of-the-art pipelines for cellular mapping in microscopy, Cellfinder[33] and Ilastik[22]. We further validated our DL models on several unseen (out-of-distribution) test datasets from different centers, demonstrating that ACE accurately segments a wide range of neuronal cell bodies of disparate size, shape and density across different imaging protocols. We apply ACE to chart local neuronal ensembles across the whole brain during (1) cold-induced food seeking and (2) movement, highlighting its generalizability across neuroscience applications.

Results

ACE algorithm, workflow and validation

Artficial intelligence-based cartography of ensembles combines DL algorithms, registration techniques and cluster-wise statistical analysis to map neuronal subtype-specific changes in whole-brain teravoxel LSFM data. Considering the importance and inherent technical complexities in segmenting neuronal somas across samples from different imaging protocols, we employed state-of-the-art DL architectures and trained them on large datasets of LSFM data from different centers. Key advances in ACE include the use of (an ensemble of) a cutting-edge vision transformer (ViT) model as its segmentation core, providing a quantitative estimate of model confidence (uncertainty) and performing cluster-wise statistical analyses via a nonparametric permutation-based algorithm.

We employed an optimized ViT as the backbone architecture for our model, which is a deep neural network designed for computer vision tasks that relies on self-attention, operating on one-dimensional (1D) flattened vectors from 3D image patches to model long-range relationships in the input data, akin to language transformers. The output of the model was obtained by ensembling the predictions of 50 models using the Monte Carlo dropout technique[35–37], to estimate model uncertainty (via computing variance across models) and enhance robustness (via averaging predictions generated from stochastically different models; Fig. 1 and Extended Data Fig. 1). For training and evaluation of ACE models, we used LSFM data acquired from 18 Tg TRAP2-Ai9 mice with the *c-fos* promoter (Extended Data Fig. 2). We divided each training dataset into smaller 3D image cubes or patches (96^3 voxels corresponding to 0.35 mm^3). To generate ground truth (GT) data for each patch, we developed a semiautomatic pipeline that relies on Ilastik[22], MIRACL[10] and FIJI/ImageJ[38]. Because the generated GT data were not obtained purely through expert manual annotation, we henceforth label these silver standard GT. We thus used 15,200 randomly selected unique input patches for training, not accounting for data augmentation (n = 30,400 with augmentation; Supplementary Fig. 1), to our knowledge providing greater than fivefold more data for training compared with DL models typically used for LSFM in the literature[39]. We tested an optimized 3D U-Net architecture (convolutional neural network, CNN) with residual blocks and dropout layers, based on our previous work[34,40], as a baseline model for comparison to our ViT model. Both architectures (ViT and U-Net) were trained and evaluated on the same image patches (Extended Data Fig. 1). We illustrate the robustness of the segmentation models on the test set and on two unseen datasets, consisting of four LSFM whole-brain datasets acquired from different centers (Extended Data Fig. 2). We highlight the differences in characteristics and distributions between the training and unseen datasets, including signal-to-noise ratio and contrast-to-noise ratio characteristics, and intensity histograms (Extended Data Fig. 2).

Artficial intelligence-based cartography of ensembles utilizes our MIRACL[10,41,42] platform to automatically register LSFM whole-brain or hemisphere data to a common coordinate system via linear and nonlinear transformations—here, ARA[43]. The segmentation maps generated at the native space of each subject are voxelized and then warped to Allen atlas resolution (Fig. 1b) using deformation fields obtained via registration. The accuracy of registration and warping can be evaluated using quality control checkpoints. Subsequently, the voxelized and warped segmentation maps are passed to the cluster-wise analysis module for statistical analysis.

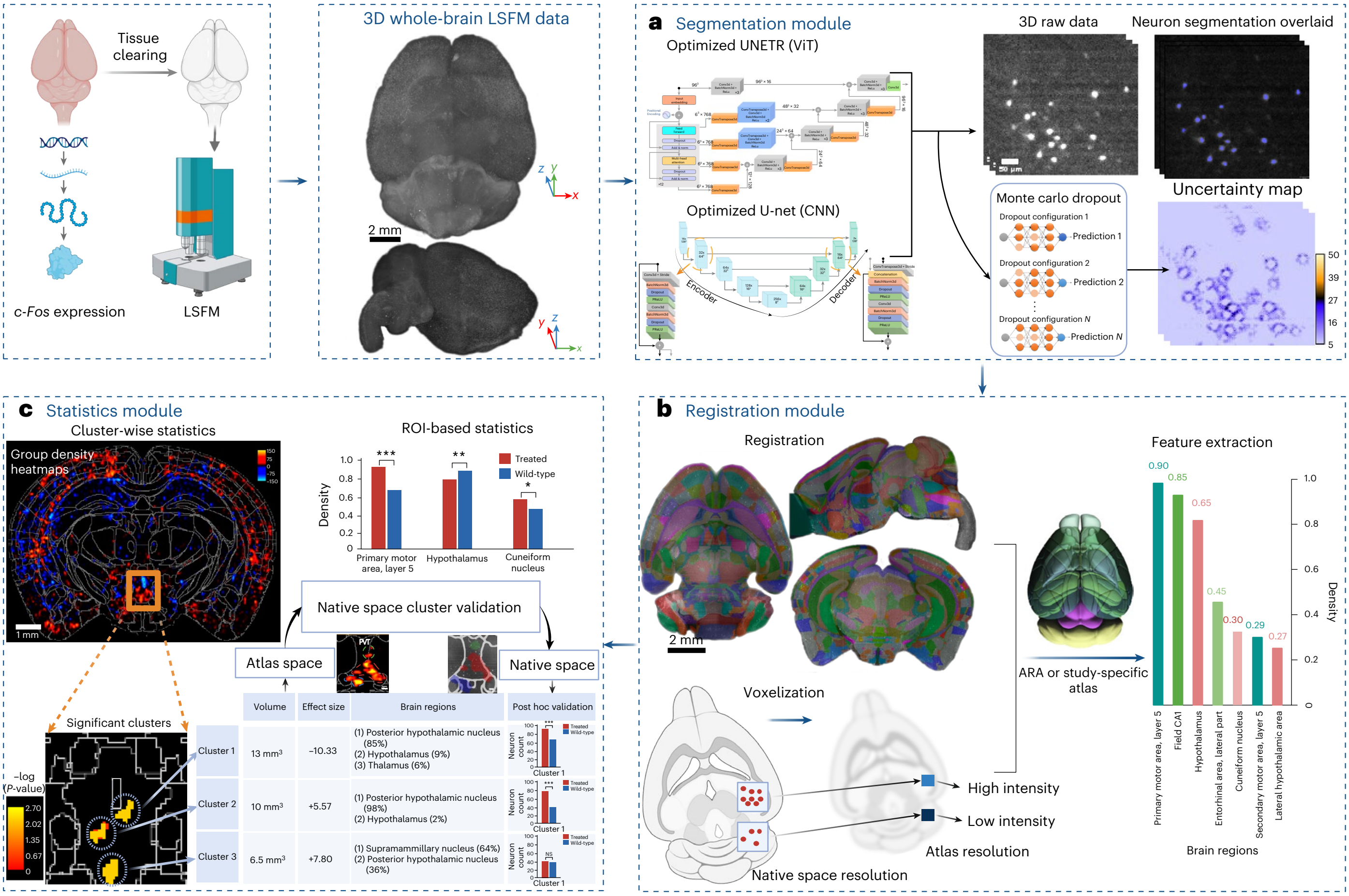

Fig. 1 | Methodological workflow of ACE. a–c, Intact whole brains immunolabeled, cleared and imaged with LSFM were used as input to the ACE pipeline. **a**, Whole-brain LSFM data are passed to ACE's segmentation module, consisting of ViT- and CNN-based DL models, to generate binary segmentation maps in addition to a voxel-wise uncertainty map for estimation of model confidence. **b**, The autofluorescence channel of data is passed to the registration module, consisting of MIRACL registration algorithms, to register to a template brain such as the Allen Mouse Brain Reference Atlas (ARA). High-resolution segmentation maps are then voxelized using a convolution filter and warped to the ARA (10 μm) using deformations obtained from registration. **c**, Voxelized and warped segmentation maps are passed to ACE's statistics module. Group-wise heatmaps of neuronal density are obtained by subtracting the average of warped and voxelized segmentation maps in each group to identify neural activity hotspots. To identify significant localized group-wise differences in neuronal activity in an atlas-agnostic manner, a cluster-wise, threshold-free cluster enhancement permutation analysis (using group-wise ANOVA) is conducted. The resulting *P* value map represents clusters showing significant differences between groups. Correspondingly, ACE outputs a table summarizing these clusters, including their volumes and the portion of each brain region included in each cluster. Significant clusters are then passed to the ACE native space cluster validation module, where clusters are warped to the native space of each subject. Utilizing warped clusters and ACE segmentation maps, the number of neurons within each cluster is calculated and a post hoc nonparametric test is applied between counts within each cluster across two groups. The top left panel of the figure was created using BioRender.com.

Artificial intelligence-based cartography of ensembles comprises a cluster-wise permutation statistics module, providing a unique capability missing in current pipelines. In an initial step, a voxel-wise statistical test (here, two-way analysis of variance (ANOVA) is applied between groups using warped segmentation maps). Next, rather than focusing on individual voxels, we consider a null hypothesis regarding the sizes of clusters in the data by incorporating the correlation structure of the data. A key advance in ACE is discovering clusters in a threshold-free approach using the threshold-free cluster enhancement (TFCE[44]) method, which enables the detection of changes in regions and subregions with higher sensitivity (Fig. 1c). Using this methodology, ACE summarizes the volume, strength (effect size) and ARA regions spanned by each cluster (Fig. 1c). Moreover, ACE extracts associations among clusters (neuronal ensembles), potentially revealing both within-region and long-range connectivity or functional coherence. Furthermore, we incorporated a native space cluster validation algorithm. This algorithm uses the cluster-wise *P* values map in atlas space, along with registration transformations, to warp clusters from atlas space into the native space of each subject for further statistical validation.

We explore the generalizability and impact of ACE by applying it in two unique neurobiological contexts. First, we identify local clusters of activations underlying food seeking following cold stress by profiling c-Fos expression in whole-brain LSFM data. Second, we identify several subregional and laminar neuronal ensembles that are differentially activated during locomotion.

Segmentation of neuronal somas in teravoxel LSFM data

We first evaluated the performance of our ViT ensemble model (using Monte Carlo dropout and *n* =50 models) on our test dataset (comprising 12,160 unique patches of 96^3 voxels ≃ 0.35 mm^3 from five animals). The high fidelity of predictions is visualized in Figs. 2a and 3a on a representative dataset, along with the corresponding GT. To quantitatively assess the performance of the models, we used a series of overlap and surface-based metrics, including recall, precision, Dice similarity coefficient (DSC) and 95% Hausdorff distance (HD_{95}).

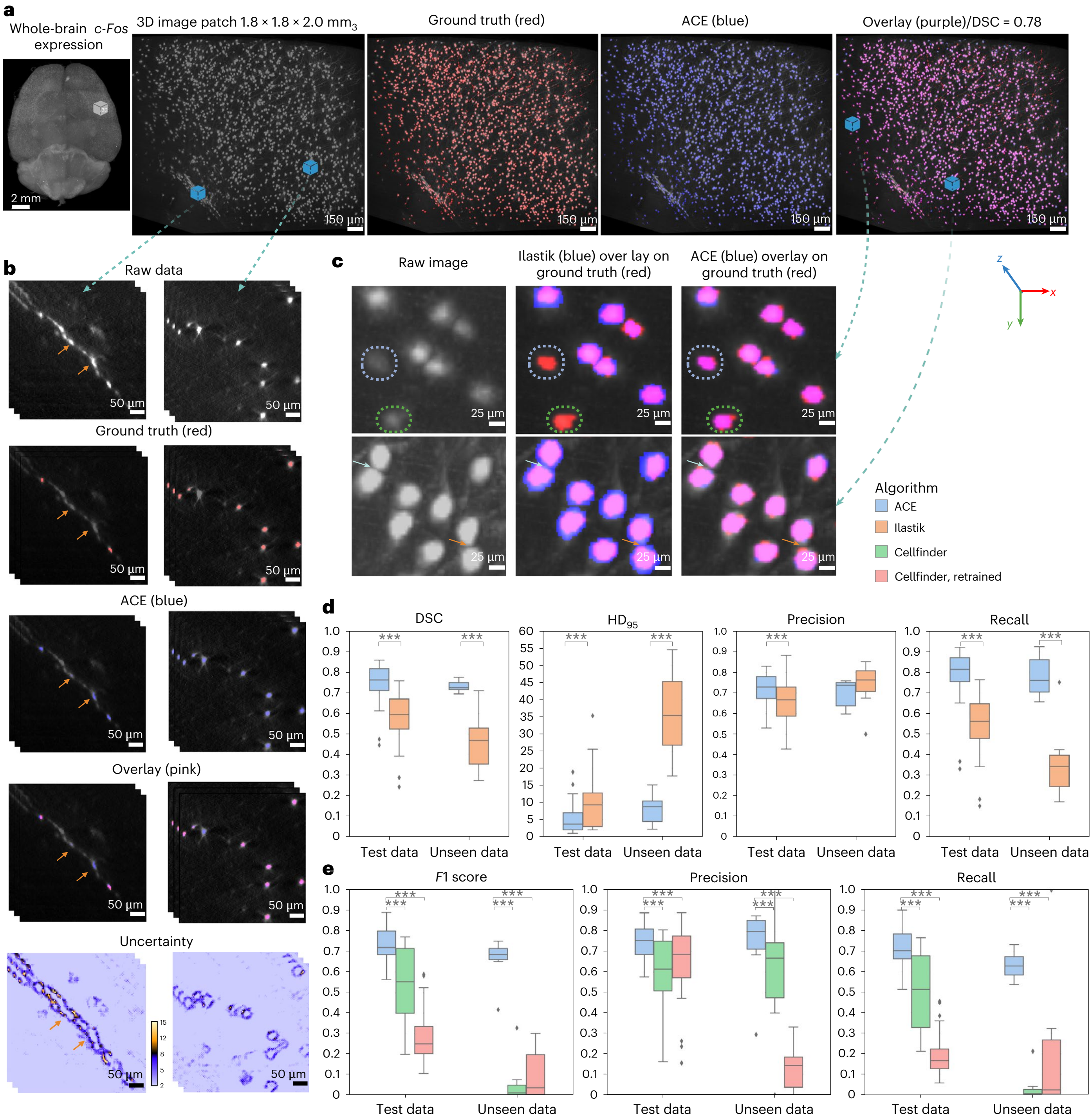

Fig. 2 | Performance of ACE in brain-wide segmentation of neuronal cell bodies. **a**, Maximum-intensity projection rendering of whole-brain c-Fos expression, with an enlarged view of a cortical patch. Segmentation maps (blue) predicted by the ViT ensemble for the enlarged subregion are shown and compared with GT (red). **b**, Raw image, GT and segmentation maps for two example image patches, along with voxel-wise uncertainty maps. Regions of high uncertainty are localized around the boundary of sparsely mislabeled processes such as axons (left-hand column) and neuronal somas (right-hand column). Arrows indicate mis-segmented regions from **a**. **c**, Qualitative evaluation of segmentation accuracy of ACE versus Ilastik in terms of detection of neurons with low signal intensity or slight blurriness (top), and their shape (bottom). Arrows indicate the boundary of two neurons close to each other. **d**,**e**, Quantitative evaluation of the segmentation accuracy of ACE versus Ilastik (**d**), and detection accuracy of ACE versus Cellfinder (**e**), in terms of average DSC, precision, recall, HD$_{95}$ and *F*1 score on test datasets ($n = 12{,}160$ unique patches with $96^3 \simeq 0.35$ mm^3) and unseen datasets ($n = 1{,}824$ unique patches of $96^3 \simeq 0.27 \times 0.27 \times 0.48$ mm^3). In box plots: box limits, upper and lower quartiles; center line, median; whiskers, 1.5× interquartile range; points, outliers. Mann–Whitney *U*-test (two-sided), ***$P < 0.0001$.

To provide a fair comparison against the state-of-the-art segmentation method, Ilastik[22], we trained an Ilastik (random forest classifier) model using patches from all training subjects. On our test set, ACE models outperformed Ilastik[22] across all experiments. ACE achieved an average improvement in DSC of 0.17 compared with the optimized Ilastik model ($P < 0.0001$, Mann–Whitney *U*-test, two-sided; Fig. 2c). ACE showed superior performance in detecting both the boundary and shape of neurons and discriminating neurons that were close to each other, resulting in a lower HD_{95} (ACE (mean ± s.d.), 4.76 ± 3.47; Ilastik, 9.60 ± 6.78; $P < 0.0001$, Mann–Whitney *U*-test, two-sided; Fig. 2c,d). Furthermore, ACE exhibited increased robustness in segmenting neurons with low signal intensity or out-of-focus blurriness (Fig. 2c), while Ilastik struggled to segment these effectively. ACE demonstrated robust segmentation accuracy across different brain regions, and consistently superior segmentation performance (on all evaluation metrics) compared with Ilastik across the whole brain (Fig. 3b and Extended Data Fig. 3). Moreover, ACE achieved higher robustness metrics in simulated distribution shifts (Gaussian noise, smoothing and sharpening) at varying severity levels compared with Ilastik (Extended Data Fig. 4).

To further validate our segmentation model, we compared its performance against the state-of-the-art detection algorithm, Cellfinder[33]. To this end, we transformed segmentation maps into detection maps by finding the center of mass of each segmented neuron. ACE exhibited superior detection performance, resulting in an *F*1 score of 0.75 ± 0.08 (mean ± s.d.) versus 0.55 ± 0.15 for Cellfinder ($P < 0.0001$, Mann–Whitney U-test, two-sided; Fig. 2e). To improve the accuracy of the Cellfinder pipeline on our dataset, we retrained (fine-tuned) the Cellfinder model on our training data and repeated the evaluation experiment. Although retraining elicited an increase of 8.64% in precision compared with the Cellfinder pretrained model, it did not improve overall performance, yielding an overall decrease in *F*1 score (to 0.28 ± 0.12).

Employing an ensemble of 50 ViTs using the Monte Carlo dropout algorithm improved our baseline model performance, resulting in an average improvement of 2.1% in precision. ACE ensemble models showed high confidence (low uncertainty) in correctly segmented regions, whereas mis-segmented regions demonstrated low confidence (high uncertainty; Fig. 2b). Areas with high uncertainty were typically observed around the boundary of neuronal somas and sparsely mislabeled processes. Voxel-wise uncertainty maps estimate segmentation confidence and can be used in postprocessing to remove potentially FP voxels.

To validate the models' generalizability, we obtained two unseen (out-of-distribution) datasets with different cell-labeling strategies (transgenic animal for training data versus routine antibody immunostaining for unseen datasets), image resolution, scanning parameters, microscope and image characteristics from those in the training dataset (Extended Data Fig. 2). From unseen dataset 1, we randomly selected 1,820 patches of 96^3 voxels each ($0.27 \times 0.27 \times 0.48$ mm^3) and generated silver standard GT data for each image patch. We employed the trained ViT ensemble model and deployed it on the unseen dataset without any fine-tuning or postprocessing (Supplementary Fig. 2). The DSC achieved by our model was 0.73 ± 0.02 (mean ± s.d.) versus 0.45 ± 0.12 for Ilastik ($P < 0.0001$, Mann–Whitney U-test, two-sided; Fig. 2d). Ilastik segmentations resulted in a substantial number of false negatives (FN) (recall (mean ± s.d.), 0.35 ± 0.15 versus 0.78 ± 0.09 for ACE, $P < 0.0001$, Mann–Whitney U-test, two-sided; Fig. 2d). Furthermore, ACE outperformed Cellfinder on this unseen dataset (with both the pretrained and fine-tuned model). To ensure a fair comparison, we further conducted Cellfinder runs using various parameters for its detection step, then selected the best model based on a visual comparison (following the authors' recommendations). This approach allowed us to account for differences in neuronal size distribution and choose the most suitable Cellfinder model for these datasets. Notwithstanding, ACE outperformed the tuned Cellfinder model on all evaluation metrics ($P < 0.0001$, Mann–Whitney U-test, two-sided; Fig. 2e). Similarly, for unseen dataset 2, the qualitative and quantitative results highlight ACE's superior performance ($P < 0.0001$, Mann–Whitney U-test, two-sided; Extended Data Fig. 5) compared with Ilastik and Cellfinder, underscoring the generalizability of our DL models to diverse imaging conditions.

To further increase ACE's robustness on unseen data, we employed an additional layer of ensembling by combining our optimized ViT and U-Net ensemble models, generating an 'ensemble of ensembles' (Supplementary Table 1 shows inference time comparison between ACE and existing algorithms). Our segmentation module thereby takes advantage of a CNN-based architecture that extracts local features within the image patch and a ViT architecture to learn long-range dependencies across the patch. The ensemble of ensembles strategy increased generalizability when dealing with the unseen dataset, improving DSC by an average of 2.1%, precision by 5.2% and decreasing average HD_{95} by 15.4%. In detection mode, ACE's ensemble of ensembles increased *F*1 score by an average of 5.1% and precision by 11.1%. Through fine-tuning of scripts, ACE is generalizable to LSFM data from other cellular markers with different morphological features compared with c-Fos (Extended Data Fig. 6a). To demonstrate the validity of this adaptation, we utilized another dataset of in situ fluorescence imaging of the targets of a covalent drug (pargyline) in intact brain tissue at the subcellular level. We randomly cropped 300 image patches with 96^3 voxels each ($0.17 \times 0.17 \times 0.19$ mm^3) from this dataset and generated silver GT data for them. We fine-tuned the ViT model on half of these patches and used the other half for evaluation. The fine-tuned ensemble model achieved a DSC of 0.74 ± 0.14 (mean ± s.d.; Extended Data Fig. 6), indicating robust performance even with different cellular markers and morphologies.

Mapping ensembles orchestrating cold-induced food seeking

Understanding the neural mechanisms governing cold-induced food seeking is crucial for unraveling the intricate interplay between environmental stimuli, energy expenditure and feeding behavior in mammals[45–47]. Our group has recently employed whole-brain c-Fos screening (via SHIELD and LSFM) of mice following prolonged (6-h) exposure to a temperature of either 4 or 30 °C ($n = 4$ per group), to map the neuronal ensembles that drive cold-induced food seeking[48]. Our findings highlight selective activation during prolonged cold exposure of the xiphoid nucleus (Xi), a small midline thalamic subregion lacking predefined ARA boundaries, suggesting that Xi plays a key role in mediation of food seeking in response to cold stress[48]. However, in this previous work, we manually identified the activation of Xi within the ventral midline thalamus based on our initial assumptions and a priori hypotheses. Notably, in this screen, we had relied on ROI-based metrics (including regions encompassing or surrounding Xi) rather than on localized statistics, due to the lack of tools able to generate cluster-wise statistical maps. Here, to validate our pipeline's ability to automatically detect selective activation of specific neuronal populations at the subregional level in an unbiased manner, we analyzed this whole-brain c-Fos LSFM dataset using ACE.

We first utilized ACE's models to generate whole-brain segmentation maps (Fig. 4a). To maintain data fidelity and prevent information loss during warping into a common reference with lower resolution, we

Fig. 3 | ROI-wise evaluation of ACE segmentation module in segmentation of neuronal cell bodies across the whole brain. a, Qualitative evaluation of ACE's segmentation module in different cortical regions in an example subject from the test dataset. Each panel from left to right demonstrates a 3D maximum-intensity projection of a raw (input) image patch, GT (red), model output (blue) and an overlaid version of all three. **b**–**d**, On the test set (in total, $n = 1,600$ unique patches $96^3 \simeq 0.35$ mm^3; minimum $n = 10$ and maximum $n = 155$ unique patches per region), we registered each LSFM dataset to the ARA using our MIRACL platform's registration algorithms. ARA labels were then warped to each subject's native space, with these warped labels then used to determine the location of each image patch in the brain. Average DSC (**b**) and HD_{95} (**c**) were obtained between ACE outputs and GT per ARA label (**d**) and compared against Ilastik. Box plots: box limits, upper and lower quartiles; center line, median; whiskers, 1.5× interquartile range; points, outliers. Mann–Whitney *U*-test (two-sided), $^{***}P < 0.001$, $^{**}P < 0.01$, $^{*}P < 0.05$. CB, cerebellum; CNU, cerebral nuclei; CTX, cerebral cortex; IB, interbrain; MB, midbrain.

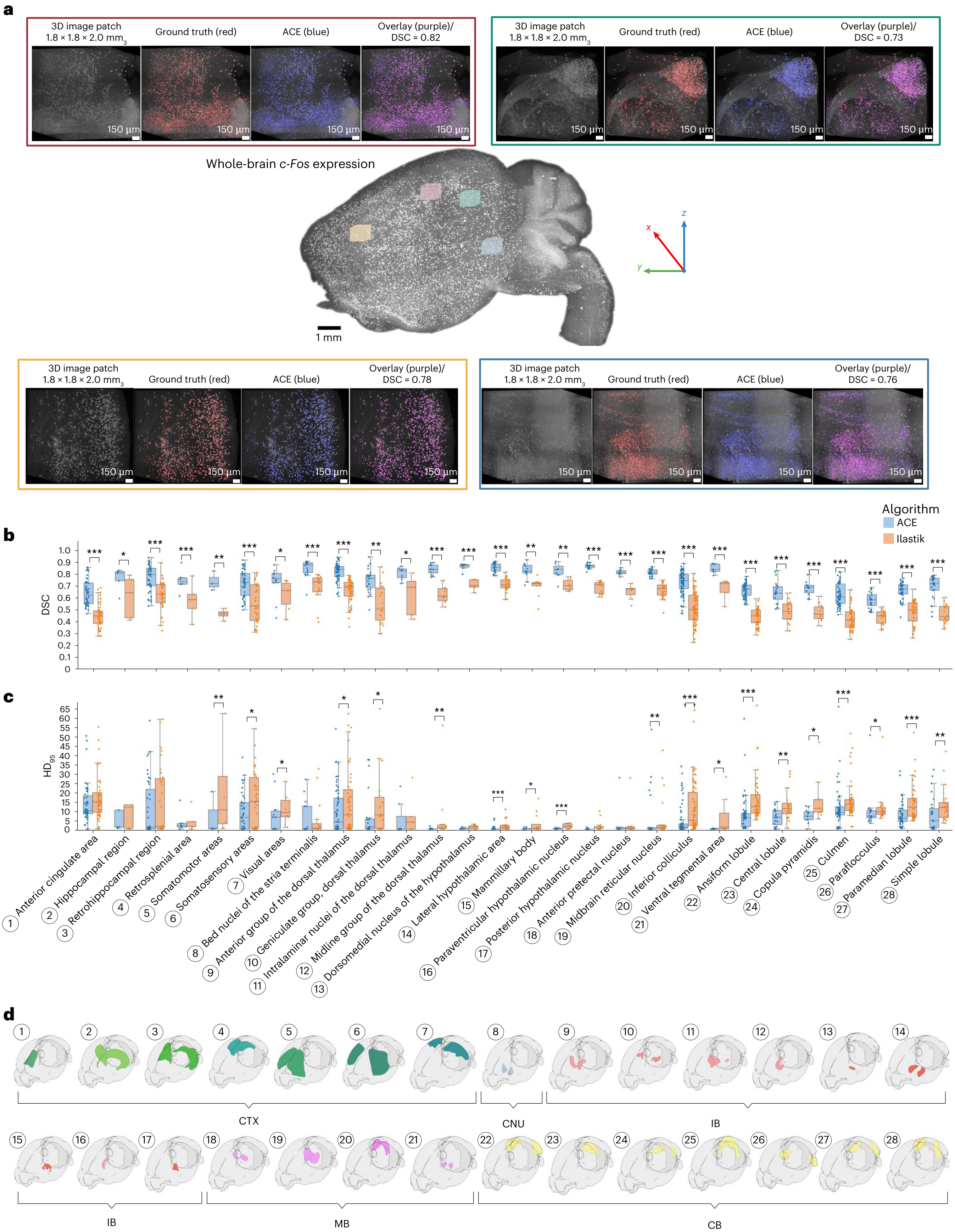
a
3D image patch 1.8 × 1.8 × 2.0 mm3
Ground truth (red)
ACE (blue)
Overlay (purple)/ DSC = 0.82
Overlay (purple)/ DSC = 0.73
Overlay (purple)/ DSC = 0.78
Overlay (purple)/ DSC = 0.76
150 µm
Whole-brain c-Fos expression
1 mm
x
y
z
b
Algorithm
ACE
Ilastik
DSC
c
HD95
1 Anterior cingulate area
2 Hippocampal region
3 Retrohippocampal region
4 Retrosplenial area
5 Somatomotor areas
6 Somatosensory areas
7 Visual areas
8 Bed nuclei of the stria terminalis
9 Anterior group of the dorsal thalamus
10 Geniculate group, dorsal thalamus
11 Intralaminar nuclei of the dorsal thalamus
12 Midline group of the dorsal thalamus
13 Dorsomedial nucleus of the hypothalamus
14 Lateral hypothalamic area
15 Mammillary body
16 Paraventricular hypothalamic nucleus
17 Posterior hypothalamic nucleus
18 Anterior pretectal nucleus
19 Midbrain reticular nucleus
20 Inferior colliculus
21 Ventral tegmental area
22 Ansiform lobule
23 Central lobule
24 Copula pyramidis
25 Culmen
26 Paraflocculus
27 Paramedian lobule
28 Simple lobule
d
CTX
CNU
IB
MB
CB

applied a convolution-based voxelization procedure to the maps based on our previous work[10]. Following voxelization, segmentation maps were aligned with ARA at 10-µm resolution using deformation fields obtained via our MIRACL platform's registration module (Fig. 4b,c and Supplementary Fig. 3). To identify neural activity hotspots, we generated group-wise heatmaps of neuronal density by subtracting the average of the voxelized and warped segmentation maps in each group (Fig. 4d). These heatmaps revealed that cold stress elicited increased neuronal activity within the hypothalamus, consistent with its role in thermoregulation[49], and attenuated neuronal activity across the cortex, probably due to reduced physical activity during cold exposure[48,50].

For assessment of between-group differences, we first conducted ROI-wise analysis between the two groups within each atlas region (Fig. 4e). This whole-brain analysis highlighted several brain regions that exhibited significant differential activation ($P < 0.05$, Student's paired t-test, two-sided), notably the paraventricular hypothalamic nucleus and the nucleus of reuniens (Fig. 4d). Some areas showed diverging group trends but did not reach significance, including the cuneiform, a region involved in locomotion[51], and primary auditory cortex. Multiple comparison corrections were not performed, following common practices of whole-brain, ROI-based analysis, due to the very large number (>1,100) of ARA regions, highlighting another key limitation of such analysis. A visual inspection of the group-difference heatmap revealed that the ROI-based analysis on predefined atlas regions failed to detect several highly localized areas with substantial increases in c-Fos activation in the cold group—most notably within the large nucleus of reuniens (Fig. 4d).

For testing of whether ACE could map localized group-wise differences in neuronal activity in an atlas-agnostic manner, we employed ACE's cluster-wise TFCE permutation test using group-wise ANOVA. ACE extracted clusters of activation across the whole brain (Fig. 4f) and summarized and ranked each cluster by its strength of activation, total volume and percentage volume within each overlapping brain region (Supplementary Table 2). Our statistical and visualization tools not only highlighted expected areas of c-Fos activation, but also identified numerous previously undetected subregional changes in the cold-induced dataset: for instance, clusters located only within the dorsal subregion of the paraventricular nucleus of the thalamus (PVT, Fig. 5), which were missed in the ROI-based analysis using the (whole) PVT region (ARA label; Fig. 4f and Supplementary Table 2). Utilizing ACE's native space cluster validation algorithm (Fig. 5 and Supplementary Table 2), we warped the clusters found in the paraventricular nucleus into the native space of each subject. We found that the number of c-Fos$^+$ cells was significantly higher (P< 0.05, Mann–Whitney U-test, two-sided; Supplementary Table 2) in the cold-induced group compared with the control group (for example, for one cluster the neuronal count in the cold-induced group was 23 ± 8 (mean ± s.d.) versus 6 ± 2 for the control). In contrast to the ROI-based analysis, our cluster-wise test revealed a significant ($P < 0.01$, group-wise two-way ANOVA; Supplementary Table 2) localized increase in c-Fos activation in the ventral midline of the nucleus of reuniens and above the third ventricle, corresponding to the Xi, and confirming its recently established role in the neural orchestration of cold-induced food-seeking behavior and energy homeostasis. We also performed connectivity analysis between significant clusters, assessing the correlation of their activations (using Pearson correlation analysis with permutation and bootstrapping; Fig. 4f). We observed significant associations ($P < 0.01$, correlation test with permutation) between clusters in the midline group of the dorsal thalamus (including paraventricular nucleus and Xi) and the nucleus accumbens—that is, putative regional connectivity, which was validated by anterograde viral tracing[48] using the Allen connectivity atlas (Fig. 4f).

Mapping of brain-wide local neuronal activation

Locomotive behavior is a complex process that involves coordinated neuronal activity in different areas of the brain[52]. Identification of laminar neuronal ensembles that underlie locomotion represents an ongoing challenge in neuroscience[1]. We deployed ACE to map local neuronal activation during walking versus homecage using c-Fos ($n = 3$ per group). Segmentation maps obtained from ACE (Extended Data Fig. 7a,b) were voxelized and warped to 10-µm ARA (Extended Data Fig. 7c). Group-wise heatmap intensity analysis (Extended Data Fig. 7d) and whole-brain ROI-based comparison showed an increase in c-Fos$^+$ density in the primary motor areas (MOp) and secondary motor areas in the walking versus homecage group ($P < 0.05$, Student's paired t-test, two-sided; Extended Data Fig. 7d). We repeated ROI-based analysis at depth 6 by merging ARA regions using the atlas's hierarchical structure (Extended Data Fig. 8a,b), a strategy used to enhance sensitivity or address lower-resolution data[53]. We identified major areas with elevated c-Fos$^+$ density, including somatomotor areas (secondary motor areas; $P < 0.05$, Student's paired t-test, two-sided). To test whether ACE could detect subregional changes, we used our cluster-wise TFCE algorithm, demonstrating layer-specific areas of c-Fos activation in both MOp and secondary motor areas (Extended Data Figs. 7e, 8c and 9 and Supplementary Table 3). We identified clusters confined to a single layer in somatomotor areas, including (1) MOp layer 6a, where thalamocortical projections from the motor thalamus were observed using anterograde viral tracing[54] and (2) clusters spanning multiple layers within the MOp and retrosplenial areas (Extended Data Figs. 8c and 9b). Notably, our algorithm (Extended Data Fig. 10) detected localized clusters in the lateral hypothalamic area (LHA) and midbrain reticular nucleus that the whole-brain and depth 6 ROI-based analyses failed to detect (Extended Data Fig. 8a,b). Using our validate clusters algorithm, we found higher LHA c-Fos$^+$ cell densities in the walking group versus homecage in the detected regions identified by ACE (Extended Data Fig. 7f and Supplementary Fig. 4), highlighting its potential role in movement.

Fig. 4 | Mapping neuronal activity underlying food seeking following cold stress. a, Experimental design ($n = 4$ per group). **b**, LSFM data were registered to the ARA using MIRACL. Left and right panels show autofluorescence data overlaid on labels for two subjects in each group. **c**, Segmentation maps from ACE were voxelized to ARA 10-µm resolution; voxelized maps were then warped to ARA. Top, one subject per group overlaid on labels; bottom, 3D rendering of segmentation maps color coded based on six regions: cerebral cortex (CTX), cerebral nuclei (CNU), midbrain (MB), hindbrain (HB), interbrain (IB) and cerebellum (CB). **d**, Segmentation maps were averaged and then subtracted to obtain group-wise heatmaps. **e**, An independent t-test (two-sided) was applied between c-Fos$^+$ density per label for ROI-wise analysis ($n = 4$ per group). Top left, trending ROIs ($P < 0.1$); top right, significant regions (***$P > 0.001$, **$P < 0.01$, *$P < 0.05$); bottom, corresponding P values per label. Box plots: box limits, upper and lower quartiles; center line, median; whiskers, 1.5× interquartile range. Data are presented as mean ± s.d. **f**, ACE cluster-wise analysis (two-way ANOVA). Top, significant clusters within the midline group of the dorsal thalamus (MTN), including one cluster close to the Xi region between the paraventricular nucleus of the hypothalamus (PVH) and above the third ventricle (left); and multiple clusters in the dorsal subregion of the paraventricular nucleus of the thalamus (PVT, right). Middle, Pearson correlation (significant correlations only, $P < 0.01$, bottom left triangle) and Euclidean distance (top right triangle) between the 22 significant clusters, ranked according to activation strength. Arrow indicates correlation between one cluster located in the nucleus of reuniens (RE) and another in the nucleus accumbens (ACB). Bottom, 3D connectivity maps derived from anterograde viral vector (AAV) tracing from an experiment (ID 184158290) in the ARA, demonstrating structural connectivity between the RE in MTN and ACB. Panels, from left to right, show (1) MTN and ACB, (2) fibers originating from RE and projecting into ACB, (3) maximum-intensity projection and (4) a sagittal view of the atlas. **a** was created using BioRender.com.

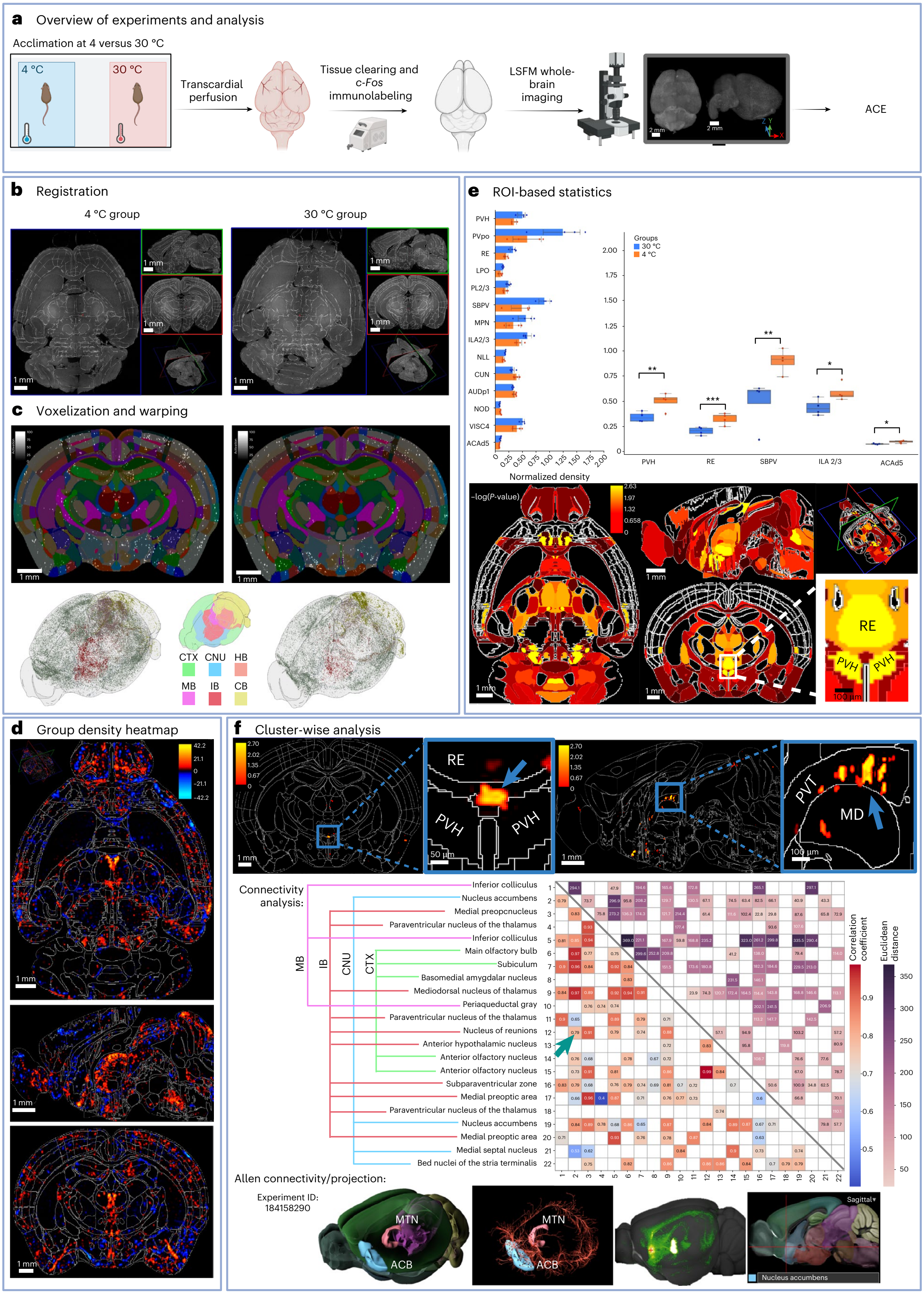
a Overview of experiments and analysis
Acclimation at 4 versus 30 °C
4 °C
30 °C
Transcardial perfusion
Tissue clearing and c-Fos immunolabeling
LSFM whole-brain imaging
2 mm
2 mm
ACE
b Registration
4 °C group
30 °C group
1 mm
c Voxelization and warping
1 mm
CTX
CNU
HB
MB
IB
CB
d Group density heatmap
42.2
21.1
0
−21.1
−42.2
1 mm
e ROI-based statistics
PVH
PVpo
RE
LPO
PL2/3
SBPV
MPN
ILA2/3
NLL
CUN
AUDp1
NOD
VISC4
ACAd5
0
0.25
0.50
0.75
1.00
1.25
1.50
1.75
2.00
Normalized density
Groups
30 °C
4 °C
**
***
**
*
*
PVH
RE
SBPV
ILA 2/3
ACAd5
−log(P-value)
2.63
1.97
1.32
0.658
0
1 mm
RE
PVH
PVH
100 μm
f Cluster-wise analysis
2.70
2.02
1.35
0.67
0
1 mm
RE
PVH
PVH
50 μm
PVT
MD
100 μm
Connectivity analysis:
MB
IB
CNU
CTX
Inferior colliculus 1
Nucleus accumbens 2
Medial preopcnucleus 3
Paraventricular nucleus of the thalamus 4
Inferior colliculus 5
Main olfactory bulb 6
Subiculum 7
Basomedial amygdalar nucleus 8
Mediodorsal nucleus of thalamus 9
Periaqueductal gray 10
Paraventricular nucleus of the thalamus 11
Nucleus of reunions 12
Anterior hypothalamic nucleus 13
Anterior olfactory nucleus 14
Anterior olfactory nucleus 15
Subparaventricular zone 16
Medial preoptic area 17
Paraventricular nucleus of the thalamus 18
Nucleus accumbens 19
Medial preoptic area 20
Medial septal nucleus 21
Bed nuclei of the stria terminalis 22
1 2 3 4 5 6 7 8 9 10 11 12 13 14 15 16 17 18 19 20 21 22
Correlation coefficient
0.9
0.8
0.7
0.6
0.5
Euclidean distance
350
300
250
200
150
100
50
Allen connectivity/projection:
Experiment ID: 184158290
MTN
ACB
MTN
ACB
Sagittal
Nucleus accumbens

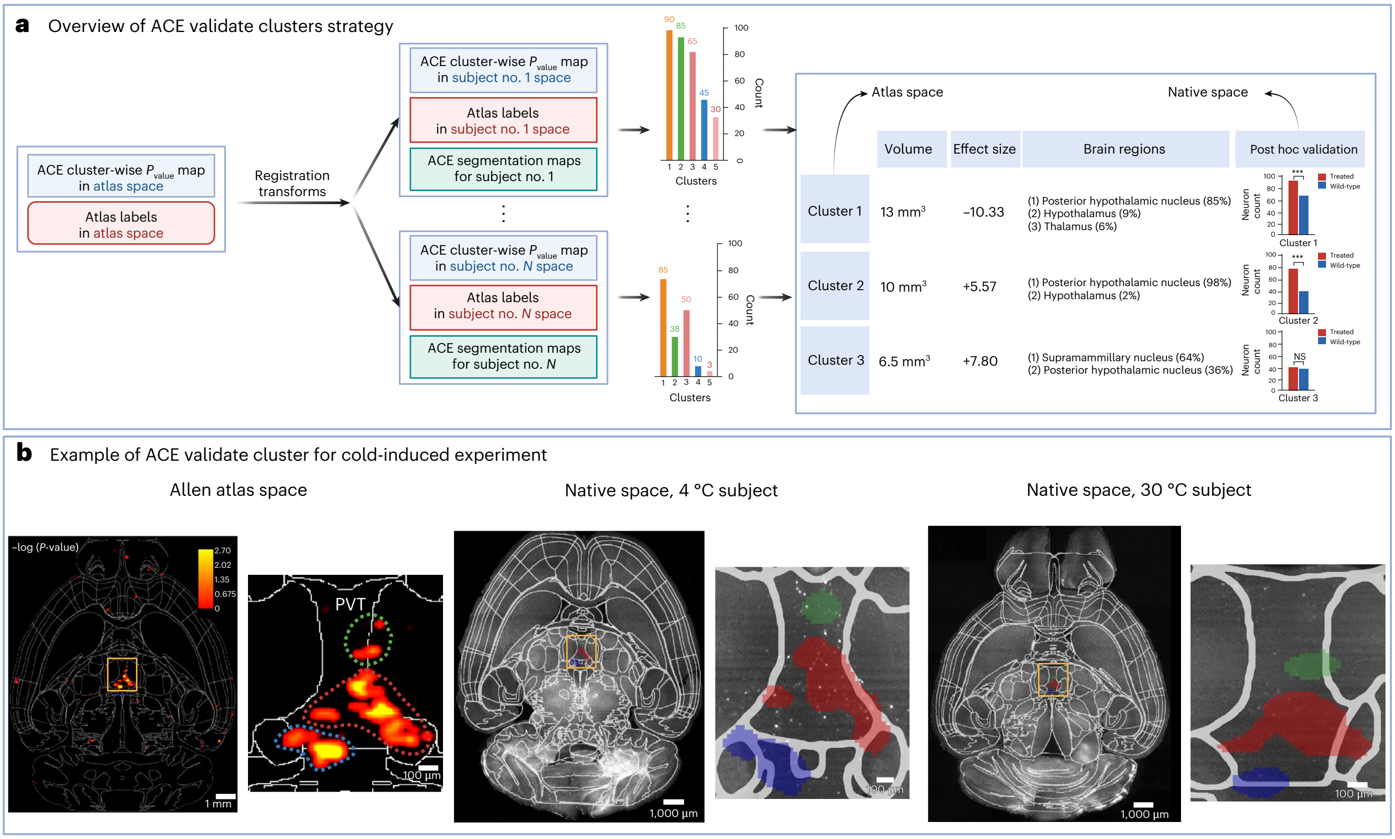
a
Overview of ACE validate clusters strategy
ACE cluster-wise P_{value} map in atlas space
Atlas labels in atlas space
Registration transforms
ACE cluster-wise P_{value} map in subject no. 1 space
Atlas labels in subject no. 1 space
ACE segmentation maps for subject no. 1
ACE cluster-wise P_{value} map in subject no. N space
Atlas labels in subject no. N space
ACE segmentation maps for subject no. N
90
85
65
45
30
Count
Clusters
85
50
38
10
3
Atlas space
Native space
Volume
Effect size
Brain regions
Post hoc validation
Cluster 1
13 mm^3
–10.33
(1) Posterior hypothalamic nucleus (85%)
(2) Hypothalamus (9%)
(3) Thalamus (6%)
Cluster 2
10 mm^3
+5.57
(1) Posterior hypothalamic nucleus (98%)
(2) Hypothalamus (2%)
Cluster 3
6.5 mm^3
+7.80
(1) Supramammillary nucleus (64%)
(2) Posterior hypothalamic nucleus (36%)
Neuron count
Treated
Wild-type
***
NS
b
Example of ACE validate cluster for cold-induced experiment
Allen atlas space
Native space, 4 °C subject
Native space, 30 °C subject
–log (P-value)
2.70
2.02
1.35
0.675
0
PVT
1 mm
100 µm
1,000 µm

Fig. 5 | ACE native space cluster validation algorithm. a, Overview of the validation algorithm. Significant clusters identified through ACE's cluster-wise TFCE permutation-based statistical algorithm were binarized and underwent a connected component analysis to differentiate each cluster. The processed significant clusters were then warped to the native space of each subject using registration deformation fields. Using ACE segmentation maps, the number of neurons within each cluster was computed. A Mann–Whitney *U*-test (two-sided) was used to compare the number of neurons within each cluster between the two groups. The number of neurons per subject for each cluster—in addition to their volume, effect size, atlas space *P* value (obtained via ACE cluster-wise TFCE permutation), brain regions they spanned and native space *P* value (obtained via post hoc Mann–Whitney *U*-test)—are summarized. **b**, Validation of neuronal ensembles detected by ACE cluster-wise analysis in the food-seeking behavior experiment. From left to right, axial view of the cluster-wise *P* value map, overlaid on ARA label boundaries at a resolution of 10 µm; zoomed view of significant clusters in PVT. The *P* value map was warped back into the native space of randomly selected subjects of the 4 and 30 ° groups using the deformation matrices obtained by registration; corresponding axial views from subjects in the 4 and 30 °C groups, respectively, and zoomed versions of cluster boundaries in PVT, showing higher c-Fos$^+$ activity in the 4 versus 30 °C condition in the clusters detected in atlas space. Cluster colors in native space (columns 2 and 3) correspond to the manually drawn boundary in atlas space (column 1), for visual comparison. NS, not significant.

Discussion

This work introduces ACE, an automated end-to-end pipeline for mapping of neuronal ensembles at the subregional level in teravoxel-scale LSFM data.

Our large training dataset and cutting-edge architectures enabled ACE models to learn variations in image characteristics of labeled cells and imaging artifacts across different regions and subjects, surpassing traditional techniques[1,21,55,56] that require parameter tuning. Due to the modular nature of the pipeline, ACE is extendable to different imaging modalities, including multiphoton microscopy data and 3D histology stacks, via fine-tuning modules available within the pipeline. Notably, ACE could be used to study connectivity via quantification of neuronal soma in upstream regions using retrograde adeno-associated virus viruses.

Our cluster-wise methodology, optimized for whole-brain LSFM data, comprehensively characterizes activity 'hotspots' while enhancing sensitivity and statistical power. Although increased FP in voxel-wise tests may be addressed through multiple correction methods[1,10,56] or manual cluster definition and subsequent post hoc analyses for validation[56], these approaches limit algorithm sensitivity. Our cluster-wise permutation analysis distinguishes itself for its automatic, data-driven cluster definition by leveraging neighborhood information, mitigating the need for data-specific expertise and minimizing bias in statistical analysis. Other key advantages to our statistical pipeline are an advanced native space cluster validation algorithm and the ability to account for covariates or perform mixed-effects modeling at the cluster level, which has not been implemented in existing tools.

When studying food seeking following cold stress, our results align with ROI-based semiautomated studies of c-Fos activation[46,48]. However, we uncovered localized changes in neural activity that may have gone unnoticed in ROI-based analyses[46,48]. ROI-based analyses may overlook subtle changes because effects, and hence significance, are estimated by averaging over the entire region. Voxel-wise methodologies are overly reliant on the intensity of individual voxels. In contrast, our approach provides a more granular understanding of neural activity patterns, offering enhanced specificity to detect nuanced changes in brain activity over small areas.

Gaining circuit-level insights based on specific neuronal populations is key to unraveling the organizational principles of the motor system[52,57]. Our findings on locomotion-elicited neuronal activity align with other studies[52], wherein c-Fos density increased in areas such as MOp and cuneiform nucleus (CUN). Our previous work, using manual parameter tuning and postprocessing of c-Fos$^+$ data, virus tracing and photostimulation, identified a subpopulation of neurons in the LHA that may play a role in walking recovery following chronic lateral hemisection spinal cord injuries. Here, we have shown increased activity restricted to a subregion localized within the LHA that probably contributed to the failure of ROI-based analysis to detect LHA activation, or remained un-noticed in studies utilizing a more limited approach of narrowing down c-Fos analysis to a few key ROIs associated with locomotion or combining ROIs into larger areas. This distinctive capability enables our pipeline to surpass the limitations of ROI-based methods, and facilitates a comprehensive and unbiased exploration of the intricate organization of brain networks.

Artficial intelligence-based cartography of ensembles provides a quantitative approach to mapping of locally activated regions in an atlas-agnostic fashion, which is particularly beneficial in experiments exploring brain areas that lack standard or high-resolution digital atlas parcellations. The resulting maps can serve as a basis for creating and refining high-fidelity functional atlases. Leveraging the statistical module and correlation analysis, ACE facilitates the extraction of associations among clusters of activations, potentially revealing long-range connectivity or functional coherence.

While this study primarily focused on the development and validation of a pipeline for mapping neuronal activity in LSFM data using immediate early genes, our fine-tuning functions allow ACE to adapt to other fluorescent reporters. However, in multilabeled datasets in which different fluorescent labels represent distinct genotypes (as seen in mosaic markers[54,58]), our fine-tuning algorithms may not produce optimal results. Although our models were trained on teravoxel LSFM, segmentation errors may still occur, biasing statistical results, particularly around sparsely mislabeled processes. This phenomenon might be, in part, attributed to the use of silver GT data; however, manual annotaton of tens of thousands of patches is impractical and unscalable. We developed the ensemble of ensembles model to deal with potential FP on unseen datasets, increasing segmentation performance. While our statistical approach using TFCE does not require predefined, cluster-forming thresholds, it utilizes free parameters. Consistent with other studies[44,59], fixing these TFCE parameters yields robust outcomes for LSFM analyses, because the same parameters were applicable to both food-seeking and walking experiments. Nevertheless, the use of suboptimal parameters may lead to an increased number of FP or FN[44,60].

In summary, ACE offers a streamlined approach for achieving high-fidelity, unbiased, 3D mapping of local and laminar neuronal ensembles across the entire brain, independent of predefined atlas regions. ACE's DL models are notable for their ability to provide generalizable segmentation of neuronal somas in teravoxel LSFM data. Integration with the MIRACL registration workflow, coupled with ACE's statistical module, establishes a framework for identifying and discovering differentially activated localized clusters of ensembles in response to experimental manipulations, which has not proved feasible to date. This comprehensive tool has the potential to empower researchers to study neural activity patterns at an unprecedented level, providing valuable insights that might be obscured using traditional ROI-based or voxel-wise analysis. ACE is applicable across a wide range of LSFM datasets and neuroscience paradigms, and is made freely available through our MIRACL platform, thus boosting our understanding of neural ensembles orchestrating behavior and cognition.

Online content

Any methods, additional references, Nature Portfolio reporting summaries, source data, extended data, supplementary information, acknowledgements, peer review information; details of author contributions and competing interests; and statements of data and code availability are available at https://doi.org/10.1038/s41592-024-02583-1.

References

1. Renier, N. et al. Mapping of brain activity by automated volume analysis of immediate early genes. *Cell* **165**, 1789–1802 (2016).
2. Kim, Y. et al. Mapping social behavior-induced brain activation at cellular resolution in the mouse. *Cell Rep.* **10**, 292–305 (2015).
3. Dyer, L., Parker, A., Paphiti, K. & Sanderson, J. Lightsheet microscopy. *Curr. Protoc.* **2**, e448 (2022).
4. Stelzer, E. H. K. Light-sheet fluorescence microscopy for quantitative biology. *Nat. Methods* **12**, 23–26 (2015).
5. Chung, K. et al. Structural and molecular interrogation of intact biological systems. *Nature* **497**, 332–337 (2013).
6. Susaki, E. A. et al. Whole-brain imaging with single-cell resolution using chemical cocktails and computational analysis. *Cell* **157**, 726–739 (2014).
7. Renier, N. et al. iDISCO: a simple, rapid method to immunolabel large tissue samples for volume imaging. *Cell* **159**, 896–910 (2014).
8. Park, Y.-G. et al. Protection of tissue physicochemical properties using polyfunctional crosslinkers. *Nat. Biotechnol.* **37**, 73–83 (2019).
9. Kim, S.-Y. et al. Stochastic electrotransport selectively enhances the transport of highly electromobile molecules. *Proc. Natl Acad. Sci. USA* **112**, E6274–E6283 (2015).
10. Goubran, M. et al. Multimodal image registration and connectivity analysis for integration of connectomic data from microscopy to MRI. *Nat. Commun.* **10**, 5504 (2019).
11. Menegas, W. et al. Dopamine neurons projecting to the posterior striatum form an anatomically distinct subclass. *eLife* **4**, e10032 (2015).
12. DeNardo, L. A. et al. Temporal evolution of cortical ensembles promoting remote memory retrieval. *Nat. Neurosci.* **22**, 460–469 (2019).
13. Herb, B. R. et al. Single-cell genomics reveals region-specific developmental trajectories underlying neuronal diversity in the human hypothalamus. *Sci. Adv.* **9**, eadf6251 (2023).
14. Ben-Simon, Y. et al. A direct excitatory projection from entorhinal layer 6b neurons to the hippocampus contributes to spatial coding and memory. *Nat. Commun.* **13**, 4826 (2022).
15. Morrone, C. D. et al. Regional differences in Alzheimer's disease pathology confound behavioural rescue after amyloid-β attenuation. *Brain* **143**, 359–373 (2020).
16. Liebmann, T. et al. Three-dimensional study of Alzheimer's disease hallmarks using the iDISCO clearing method. *Cell Rep.* **16**, 1138–1152 (2016).
17. Gómez-Isla, T. et al. Profound loss of layer II entorhinal cortex neurons occurs in very mild Alzheimer's disease. *J. Neurosci.* **16**, 4491–4500 (1996).
18. Jeon, S. G., Kim, Y. J., Kim, K. A., Mook-Jung, I. & Moon, M. Visualization of altered hippocampal connectivity in an animal model of Alzheimer's disease. *Mol. Neurobiol.* **55**, 7886–7899 (2018).
19. Eklund, A., Nichols, T. E. & Knutsson, H. Cluster failure: why fMRI inferences for spatial extent have inflated false-positive rates. *Proc. Natl Acad. Sci. USA* **113**, 7900–7905 (2016).
20. Benjamini, Y. & Hochberg, Y. Controlling the false discovery rate: a practical and powerful approach to multiple testing. *J. R. Stat. Soc. Series B Stat. Methodol.* **57**, 289–300 (1995).
21. Fürth, D. et al. An interactive framework for whole-brain maps at cellular resolution. *Nat. Neurosci.* **21**, 139–149 (2018).
22. Berg, S. et al. Ilastik: interactive machine learning for (bio)image analysis. *Nat. Methods* **16**, 1226–1232 (2019).
23. Mahony, N. O. et al. Deep learning vs. traditional computer vision. Preprint at https://arxiv.org/abs/1910.13796 (2019).

24. Wang, L.-W. et al. A weakly supervised U-Net model for precise whole brain immunolabeled cell detection. Preprint at *bioRxiv* https://doi.org/10.1101/2023.03.16.531434 (2023).
25. Moen, E. et al. Deep learning for cellular image analysis. *Nat. Methods* **16**, 1233–1246 (2019).
26. Kromp, F. et al. Evaluation of deep learning architectures for complex immunofluorescence nuclear image segmentation. *IEEE Trans. Med. Imaging* **40**, 1934–1949 (2021).
27. Stringer, C., Wang, T., Michaelos, M. & Pachitariu, M. Cellpose: a generalist algorithm for cellular segmentation. *Nat. Methods* **18**, 100–106 (2021).
28. Pachitariu, M. & Stringer, C. Cellpose 2.0: how to train your own model. *Nat. Methods* **19**, 1634–1641 (2022).
29. Schmidt, U., Weigert, M., Broaddus, C. & Myers, G. in *Medical Image Computing and Computer Assisted Intervention – MICCAI 2018* (eds Frangi, A. F. et al.) 265–273 (Springer International Publishing, 2018).
30. Haberl, M. G. et al. CDeep3M—plug-and-play cloud-based deep learning for image segmentation. *Nat. Methods* **15**, 677–680 (2018).
31. Lugagne, J.-B., Lin, H. & Dunlop, M. J. DeLTA: automated cell segmentation, tracking, and lineage reconstruction using deep learning. *PLoS Comput. Biol.* **16**, e1007673 (2020).
32. Iqbal, A., Sheikh, A. & Karayannis, T. DeNeRD: high-throughput detection of neurons for brain-wide analysis with deep learning. *Sci. Rep.* **9**, 13828 (2019).
33. Tyson, A. L. et al. A deep learning algorithm for 3D cell detection in whole mouse brain image datasets. *PLoS Comput. Biol.* **17**, e1009074 (2021).
34. Mojiri Forooshani, P. et al. Deep Bayesian networks for uncertainty estimation and adversarial resistance of white matter hyperintensity segmentation. *Hum. Brain Mapp.* **43**, 2089–2108 (2022).
35. Kendall, A. & Gal, Y. in *Advances in Neural Information Processing Systems* (Curran Associates, Inc., 2017).
36. Gal, Y. & Ghahramani, Z. Dropout as a Bayesian approximation: representing model uncertainty in deep learning. *Proc. Mach. Learn. Res.* **48**, 1050–1059 (2016).
37. Avci, M. Y. et al. Quantifying the uncertainty of neural networks using Monte Carlo dropout for deep learning based quantitative MRI. Preprint at https://doi.org/10.48550/arXiv.2112.01587 (2021).
38. Schindelin, J. et al. Fiji: an open-source platform for biological-image analysis. *Nat. Methods* **9**, 676–682 (2012).
39. Kaltenecker, D. et al. Virtual reality-empowered deep-learning analysis of brain cells. *Nat. Methods* **21**, 1306–1315 (2024).
40. Goubran, M. et al. Hippocampal segmentation for brains with extensive atrophy using three-dimensional convolutional neural networks. *Hum. Brain Mapp.* **41**, 291–308 (2020).
41. Hsueh, B. et al. Cardiogenic control of affective behavioural state. *Nature* **615**, 292–299 (2023).
42. Boillat, M. et al. Neuroinflammation-associated aspecific manipulation of mouse predator fear by *Toxoplasma gondii*. *Cell Rep.* **30**, 320–334 (2020).
43. Wang, Q. et al. The Allen Mouse Brain Common Coordinate Framework: a 3D reference atlas. *Cell* **181**, 936–953 (2020).
44. Smith, S. M. & Nichols, T. E. Threshold-free cluster enhancement: addressing problems of smoothing, threshold dependence and localisation in cluster inference. *NeuroImage* **44**, 83–98 (2009).
45. Zhao, Z. et al. Effects of ambient temperatures between 5 and 35 °C on energy balance, body mass and body composition in mice. *Mol. Metab.* **64**, 101551 (2022).
46. Qian, S. et al. A temperature-regulated circuit for feeding behavior. *Nat. Commun.* **13**, 4229 (2022).
47. Deem, J. D. et al. Cold-induced hyperphagia requires AgRP neuron activation in mice. *eLife* **9**, e58764 (2020).
48. Lal, N. K. et al. Xiphoid nucleus of the midline thalamus controls cold-induced food seeking. *Nature* **621**, 138–145 (2023).
49. Labbé, S. M. et al. Hypothalamic control of brown adipose tissue thermogenesis. *Front. Syst. Neurosci.* **9**, 150 (2015).
50. Barnett, S. A. Adaptation of mice to cold. *Biol. Rev.* **40**, 5–51 (1965).
51. Fougère, M. et al. Optogenetic stimulation of glutamatergic neurons in the cuneiform nucleus controls locomotion in a mouse model of Parkinson's disease. *Proc. Natl Acad. Sci. USA* **118**, e2110934118 (2021).
52. Arber, S. & Costa, R. M. Connecting neuronal circuits for movement. *Science* **360**, 1403–1404 (2018).
53. Cai, Y., Zhang, X., Li, C., Ghashghaei, H. T. & Greenbaum, A. COMBINe enables automated detection and classification of neurons and astrocytes in tissue-cleared mouse brains. *Cell Rep. Methods* **3**, 100454 (2023).
54. Lee, C., Kim, Y. & Kaang, B.-K. The primary motor cortex: the hub of motor learning in rodents. *Neuroscience* **485**, 163–170 (2022).
55. Wang, X. et al. Bi-channel image registration and deep-learning segmentation (BIRDS) for efficient, versatile 3D mapping of mouse brain. *eLife* **10**, e63455 (2021).
56. Rijsketic, D. R. et al. UNRAVELing the synergistic effects of psilocybin and environment on brain-wide immediate early gene expression in mice. *Neuropsychopharmacology* **48**, 1798–1807 (2023).
57. Kathe, C. et al. The neurons that restore walking after paralysis. *Nature* **611**, 540–547 (2022).
58. Beattie, R. et al. Mosaic analysis with double markers reveals distinct sequential functions of Lgl1 in neural stem cells. *Neuron* **94**, 517–533 (2017).
59. Salimi-Khorshidi, G., Smith, S. M. & Nichols, T. E. Adjusting the effect of nonstationarity in cluster-based and TFCE inference. *NeuroImage* **54**, 2006–2019 (2011).
60. Spisák, T. et al. Probabilistic TFCE: a generalised combination of cluster size and voxel intensity to increase statistical power. *NeuroImage* **185**, 12–26 (2019).

Publisher's note Springer Nature remains neutral with regard to jurisdictional claims in published maps and institutional affiliations.

[1]Department of Medical Biophysics, University of Toronto, Toronto, Ontario, Canada. [2]Physical Sciences, Sunnybrook Research Institute, Toronto, Ontario, Canada. [3]Hurvitz Brain Sciences, Sunnybrook Health Sciences Centre, Toronto, Ontario, Canada. [4]Department of Neuroscience, Dorris Neuroscience Center, The Scripps Research Institute, San Diego, CA, USA. [5]Department of Molecular Medicine, The Scripps Research Institute, La Jolla, CA, USA. [6]Defitech Center for Interventional Neurotherapies (.NeuroRestore), CHUV/UNIL/EPFL, Lausanne, Switzerland. [7]NeuroX Institute, School of Life Sciences, Swiss Federal Institute of Technology (EPFL), Lausanne, Switzerland. [8]Department of Neurosurgery, Lausanne University Hospital (CHUV) and University of Lausanne (UNIL), Lausanne, Switzerland. [9]Biological Sciences, Sunnybrook Research Institute, Toronto, Ontario, Canada. [10]Department of Laboratory Medicine & Pathobiology, University of Toronto, Toronto, Ontario, Canada. [11]Department of Bioengineering, Stanford University, Stanford, CA, USA. [12]Howard Hughes Medical Institute, Stanford University, Stanford, CA, USA. [13]Harquail Centre for Neuromodulation, Sunnybrook Health Sciences Centre, Toronto, Ontario, Canada. [14]These authors jointly supervised this work: Bojana Stefanovic, Maged Goubran. ✉e-mail: maged.goubran@utoronto.ca

Methods

Datasets and experiments

Training dataset. Our training data consisted of two LSFM cohorts of TRAP2-Ai9 mice (total $n = 18$): (1) ten animals aged 3–4 months with whole-brain data acquired and (2) eight animals aged 2 months with data acquired from the left hemisphere. All animal procedures followed animal care guidelines approved by the Institutional Animal Care and Use Committee at the Scripps Research Institute. These animals had an immediate early gene (*c-fos*) promoter, contributing to the activity-dependent expression of inducible recombinase Cre-ERT2. The expression of fluorescent protein tdTomato was activated following the injection of 20 mg kg^{-1} 4-hydroxytamoxifen. We used the following splits for training and evaluation: the training set consisted of ten animals, with three and five used for the validation and test sets, respectively.

Unseen dataset 1. We used whole-brain LSFM data from a model of spinal cord injury ($n = 3$ mice) to validate our DL segmentation models. Briefly, mice were induced under anesthesia with a mixture of isoflurane and O_2. Mice were then placed on a heating pad set to 37 °C and maintained on 1–3% isoflurane and O_2. A midline skin incision was made and the T10 lamina identified. A T10 laminectomy was performed, followed by left lateral hemisection using either microscissors or a microscalpel[61]. Muscle closure was performed with 6-0 Vicryl followed by skin closure with 6-0 Ethilon. Postoperatively, mice were placed on a heating pad and given subcutaneous fluids as needed. Pain control for 48 h postoperatively was also provided via subcutaneous daily administration of Rimadyl (5 mg/kg^{-1}). Bladders were expressed twice daily until spontaneous recovery of bladder function. All hemisection lesions were histologically confirmed as adequate. All three mice were adult female C57BL/6 mice (≥8 weeks of age at the start of the experiment, 15–30 g body weight). All procedures were performed in compliance with the Swiss Veterinary Law guidelines and were approved by the Veterinary Office of the Canton of Geneva, Switzerland (license no. GE/112/20).

Unseen dataset 2. We used whole-brain LSFM data obtained from a male C57BL/6 J mouse (Jackson Laboratory, strain 000664), aged 18 months. All animal procedures followed protocols approved by the Stanford University Institutional Animal Care and Use Committee, and met the guidelines of the National Institutes of Health Guide for the Care and Use of Laboratory Animals.

Cold dataset. We analyzed the cold and thermoneutral c-Fos dataset from our previous publication[48]. Briefly, single-housed male wild-type (WT) C57BL/J6 mice were exposed to either 4 °C (cold) or 30 °C (thermoneutral) for 6 h, with free access to food and water, before perfusion. Mouse brains were harvested and fixed in 4% paraformaldehyde (PFA) following perfusion.

Walking dataset. We used two groups of adult female C57BL/6 mice (≥8 weeks of age at the start of the experiment, 15–30 g body weight, $n = 3$ per group). Briefly, mice were trained to run quadrupedally on a treadmill (Robomedica, Inc.) 5 days per week for 2 weeks before perfusion. To elicit c-Fos expression, mice ran on the treadmill for 45 min at a speed of 9 cm s^{-1} and were then perfused for 1 h (walking group). Mice in their home cages were perfused for homecage group analysis.

Fine-tuning dataset. We used LSFM data from a hemisphere of a mouse brain. The clearing-assisted tissue click chemistry method was used for in situ fluorescence imaging of drug molecules that bind to specific targets. In this method, the covalent monoamine oxidase inhibitor pargyline-yne was administered to the mouse at a dose of 10 mg kg^{-1} for 1 h by intraperitoneal injection. The drug was labeled with AF647 dye using a click reaction, allowing us to visualize drug molecules within brain tissue.

Tissue clearing and immunolabeling

Training dataset. Two weeks following injection of 4-hydroxy tamoxifen, mice were perfused; their brains were collected and underwent overnight fixation in 4% PFA solution. Fixed brain specimens were treated using the SHIELD[8] protocol to maintain the integrity of protein antigenicity. Thereafter, an active clearing procedure was used for tissue CLARITY[5]. Samples were index matched by adding them to EasyIndex medium before imaging with a light-sheet microscope.

Unseen dataset 1 and walking dataset. Adult mice were anesthetized with intraperitoneal pentobarbital (150 mg kg^{-1}), followed by intracardiac perfusion of 1× PBS then 4% PFA in PBS. The brain was dissected and the sample postfixed in 4% PFA overnight at 4 °C. Brains then underwent processing with iDISCO+ (ref. 1). Briefly, samples underwent methanol pretreatment by dehydration with a methanol/H_2O series, each for 1 h, as follows: 20, 40, 60, 80 and 100%. Samples were then washed with 100% methanol for 1 h and chilled at 4 °C, followed by overnight incubation in 66% dichloromethane/33% methanol at room temperature. This was followed by two washes in 100% methanol at room temperature, then bleaching in chilled fresh 5% H_2O_2 in methanol overnight at 4 °C. Samples were rehydrated with a methanol/H_2O series as follows: 80, 60, 40 and 20% then PBS, each for 1 h at room temperature. Samples underwent washing for 2× 1 h at room temperature in PTx.2 buffer, and were then incubated in permeabilization solution for 2 days at 37 °C. Samples were then incubated in blocking solution (42 ml of PTx.2, 3 ml of normal donkey serum and 5 ml of DMSO, for a total stock volume of 50 ml) for 2 days at 37 °C with shaking. This was followed by incubation in a primary antibody solution consisting of PBS/0.2% Tween-20 with 10 µg/ml heparin (PTwH), 5% DMSO, 3% normal donkey serum and c-Fos (rabbit anti-c-Fos, 1:2,000, Synaptic Systems, catalog no. 226003) for 7 days at 37 °C with shaking. Next, samples were washed in PTwH for 24 h, followed by incubation in a secondary antibody solution consisting of PTwH, 3% normal donkey serum and donkey anti-rabbit Alexa Fluor 647 (1:500, Thermo Fisher Scientific) for 7 days at 37 °C with shaking. Samples were then washed in PTwH for 24 h, followed by tissue clearing; final clearing was performed using iDISCO+ (ref. 1). Briefly, samples were dehydrated in a methanol/H_2O series as follows: 20, 40, 60, 80 and 100%, each 2× 1 h at room temperature. This was followed by a 3-h incubation in 66% dichloromethane/33% methanol at room temperature, then incubation in 100% dichloromethane for 2× 15 min. Samples were then incubated in dibenzyl ether for at least 24 h before imaging.

Cold dataset. Whole-brain clearing was performed by LifeCanvas Technologies through a contracted service. To preserve samples' protein architecture, they were fixed with proprietary SHIELD[8] solutions from LifeCanvas Technologies. Samples were then placed in the SmartBatch+ system to carry out active clearing and immunolabeling with rabbit anti-c-Fos primary antibody (CST, catalog no. 2250S). Samples were index matched by placing them in EasyIndex medium.

Unseen dataset 2. The animal was anesthetized with isoflurane and transcardially perfused with PBS, followed by 4% PFA. The whole mouse brain was extracted carefully and fixed in 4% PFA for 24 h; the PFA-fixed sample was then processed using the SHIELD[8] protocol (LifeCanvas Technologies). Active clearing of samples was carried out using the Smartbatch+ device. Samples were then immunolabeled using eFLASH[62] technology, incorporating the electrotransport and SWITCH[63] methods. Samples were labeled with a recombinant anti-c-Fos antibody (abcam, catalog no. ab214672) and then fluorescently conjugated with Alexa Fluor 647 (Invitrogen, catalog no. A-31573) at a primary:secondary molar ratio of 1.0:1.5. Following labeling, samples were index matched ($n = 1.52$) by incubation in EasyIndex medium (LifeCanvas Technologies).

LSFM imaging

Training dataset. Samples were index matched with EasyIndex medium and imaged on a light-sheet microscope (SmartSPIM) with a ×4 objective lens. For eight subjects, data were acquired from a hemisphere while, for the remainder, data were acquired from the whole brain. Nominal lateral spatial resolution was 3.5 µm, and step size was set to 4 µm in the *z*-direction, with 561-nm excitation and an emission filter of 600/52 nm.

Unseen dataset 1 and walking dataset. Imaging of whole brains was performed using a CLARITY-optimized light-sheet microscope, as previously described[64], with a pixel resolution of $1.4 \times 1.4\ \mu\mathrm{m}^2$ in the *x* and *y* dimensions and a *z*-step of 5 µm, respectively, using the ×4/0.28 (numerical aperture) objective, which is suitable for resolving cell nuclei labeled by c-Fos. Using a custom-made quartz cuvette filled with dibenzyl ether, whole brains were imaged. Two channels were imaged: one with autofluorescence (auto channel, 488 nm) to demonstrate anatomy, and a second demonstrating c-Fos labeling (cell channel, 647 nm). All raw images were acquired as 16-bit TIFF files and were stitched together using TeraStitcher[65].

Cold dataset. Whole-brain imaging and automated analysis were performed by LifeCanvas Technologies through a contracted service. Samples were index matched by placing them in EasyIndex medium, and imaged on a light-sheet microscope (SmartSPIM) with a ×4 objective lens. Nominal lateral spatial resolution was 1.75 µm, and step size was set to 4 µm in the *z*-direction.

Unseen dataset 2. The index-matched ($n = 1.52$) whole-brain sample was imaged using a SmartSPIM light-sheet microscope. The sample was imaged with a ×4 objective lens. Samples were imaged with a 642-nm laser. Nominal lateral spatial resolution was 1.8 µm, and step size was set to 4 µm in the *z*-direction

GT label generation

Our annotation strategy for generating silver standard GT labels of neuronal somas comprised three stages: MIRACL[10] segmentation, Ilastik pixel classification and postprocessing.

MIRACL segmentation. To create GT labels, we first used the MIRACL[10] segmentation workflow that incorporates image-processing tools implemented as FIJI/ImageJ macros[38]. The workflow includes a 3D watershed marker-controlled algorithm and a postprocessing 3D shape filter to omit FP. This resulted in binary GT labels across the entire dataset with a low FP rate and relatively higher FN rate.

Ilastik pixel classification. To improve MIRACL-generated GT labels we used Ilastik[22], which performs pixel classification using image filters (as input features) and a random forest (RF) algorithm (as a classifier) through a user-friendly interface. Filters include pixel color and intensity descriptors, edginess and texture in 3D and at different scales. The RF combines hundreds of decision trees and trains each one on a slightly different set of features. The final predictions of RF are made by averaging the predictions of each tree. We used 37 three-dimensional filters and an RF classifier with 100 trees. To train the RF classifier, we imported MIRACL's segmentation outputs as silver input annotations (initialization) to Ilastik (that is, in lieu of manual annotations). To address the prohibitive speed and memory requirements of the RF algorithm, we trained it on image patches (512^3 voxels). For each brain, three 512^3 patches from different depths were randomly selected. The RF model was trained several times by providing feedback (that is, by correcting the results with expert annotation and modifying the labels to achieve optimal results). Ilastik output did not correctly detect the boundaries of neuronal soma, and frequently overestimated their spatial extent.

Postprocessing. To further reduce the number of FP voxels in GT labels, we applied a 3D shape filter using the ImageJ shape filter plugin[66] on Ilastik-generated labels. To solve the problem of volume overestimation, we applied a 3D erosion filter with a sphere-like kernel (radius of one voxel) to the GT labels. The final whole-brain GT labels were visually quality checked in three 512^3 patches per brain, by two raters; specifically, the raters were asked to randomly select and validate one 512^3 patch in the cerebrum, brain stem and cerebellum.

Deep neural network architectures

ACE's segmentation module consisted of 3D ViT-based and CNN-based (U-Net) architectures (Extended Data Fig. 1).

UNETR. The popular U-Net architecture has powerful representation learning capabilities, and generates more accurate dense-segmentation masks than do other CNN architectures (such as Mask R-CNN), thanks to the preservation of spatial information[26,67]. However, fully convolutional models are limited in their ability to learn long-range dependencies, resulting in potentially suboptimal segmentation of objects in large volumes, including neuronal cell bodies of varying shape and size (for example, in different regions of the brain). To address this issue, a ViT architecture (UNETR) has been proposed in which the encoder path of a U-Net is replaced by a transformer to learn contextual information from the embedded input patches[68]. This motivated us to develop and deploy optimized UNETR-based segmentation models with residual blocks and dropout layers to improve the robustness and generalizability of previous pipelines. Specifically, in UNETR[68] the encoder was replaced with a stack of 12 transformer blocks, operating on a 1D sequence ($16^3 = 4{,}096$) embedding of the input (one channel 3D image patch, $96^3 \simeq 0.27 \times 0.27 \times 0.48\ \mathrm{mm}^3$). Subsequently, a linear layer projected the vectors into a lower dimensional embedding space (embedding size $K = 768$), which remained constant throughout the transformer layers. A 1D learnable positional embedding was added to the projected patch sequence to preserve spatial information. This embedded patch sequence, with the dimension of $N \times K$ (N is the sequence length and $N = H/16 \times W/16 \times D/16 \times K$ and H, W and D are the 3D input's height, width and depth), was passed as input to the stack of transformer blocks. Each transformer block consisted of multihead attention and multilayer perceptron layers. All multihead attention modules consisted of multiple self-attention heads, where each self-attention block learned mapping in the patch sequence in parallel. We extracted learned sequence representations at four different depths of the transformer stack and reshaped each back to $\frac{H}{16} \times \frac{W}{16} \times \frac{D}{16} \times K$. The embedded sequence vectors then underwent five different encoder blocks with consecutive convolutional layers to achieve supervision at different depths (Extended Data Fig. 1).

The encoder was connected to a decoder via skip connections at multiple resolutions, to predict segmentation outputs. We developed an optimized UNETR[68] architecture with some modifications, including the addition of dropout layers in all blocks and residual units[69] in convolution blocks in the encoder, as a regularization strategy to avoid overfitting and vanishing gradient problems. For a given 3D input cube, the segmentation models generated a 3D volume containing voxel-wise probabilities of neuronal cell bodies ($0 < P < 1$). Prediction maps were binarized using either a default (0.5) or user-fed threshold to generate a map representing whether a voxel belongs to a neuron.

U-Net. We similarly implemented an optimized version of the seminal U-Net[70–72] architecture, with some modifications, based on our previous work[40]. The U-Net architecture consists of contracting (encoder) and expanding (decoder) paths. The encoder is based on 3D convolution and pooling operators; it takes an image patch as input and generates feature maps at various scales, creating a multilevel, multiresolution feature representation. Meanwhile, the decoder with up-convolution operators leverages these feature representations to classify all pixels at the original image resolution. The decoder assembles the segmentation, starting with low-resolution feature maps that capture large-scale structures, and gradually refines the output to include fine-scale details. In our U-Net architecture, the standard building blocks have been replaced with a residual block[69]. In addition, parametric rectifying linear units[73] have been deployed to provide different parameterized nonlinearity for different layers. We converted all 2D operations, including convolution and max-pooling layers, into 3D and used batch normalization rather than instance normalization to achieve a stable distribution of activation values throughout the training, and to accelerate training[74]. A dropout layer was added between all convolution blocks in the architecture as a regularizer, to avoid overfitting[36,75]. Except for the first residual units, all convolutions and transpose convolutions had a stride of 2 for downsampling and upsampling, respectively. The first residual unit used a stride of 1, which has been shown to increase performance by not immediately downsampling the input image patch[70].

All brain light-sheet data are first divided into smaller image patches. Deploying ACE segmentation models, binary and uncertainty maps are obtained per image patch; the pipeline then automatically stitches all the maps to create whole-brain segmentation and uncertainty maps that match the input data.

Loss function

The DSC is a widely used metric that measures similarity between two labels. The class average of the DSC can be computed as

$$D(\mathrm{GT},P) = \frac{2}{N}\sum_{n=1}^{N}\frac{\sum_{k=1}^{K}\mathrm{GT}_{k,n}P_{k,n}}{\sum_{k=1}^{K}\mathrm{GT}_{k}^{2}+\sum_{k=1}^{K}P_{k}^{2}},$$

where N is the number of classes, K is the number of voxels and $\mathrm{GT}_{k,n}$ and $P_{k,n}$ denote GT and output prediction, respectively, for class n at voxel k.

Cross-entropy (CE) measures the difference between two probability distributions over the same sets of underlying events, and was computed as

$$\mathrm{CE}(\mathrm{GT},P) = \frac{1}{K}\sum_{k=1}^{K}\sum_{n=1}^{N}\mathrm{GT}_{k,n}\log(P_{k,n}).$$

In regard to ACE DL architecture, we used an equally weighted Dice–cross-entropy loss, which is a combination of Dice loss and cross-entropy loss functions; this was computed in a voxel-wise manner as

$$L(\mathrm{GT},P) = D(\mathrm{GT},P) + \mathrm{CE}(\mathrm{GT},P).$$

Model training

To train our DL models, we used a total of 36,480 unique input patches (96^3 voxels), not accounting for data augmentation. To address the issue of class imbalance in our dataset (the majority of voxels representing background), patches containing only background—or a small number of foreground voxels (<100,000)—were filtered out from the 512^3 image patches generated by the annotation strategy. Hence, for the UNETR model with an input size of 96^3, we used 15,200, 9,120 and 12,160 unique input patches (not accounting for data augmentation) for training, validation and testing, respectively ($n = 30{,}400$ patches with augmentation for training alone); for the U-Net model with an input size of 128^3, we used 7,600, 3,840 and 5,120 patches, respectively.

For hyperparameter tuning, we used a Bayesian optimization approach via the Adaptive Experimentation Platform (https://ax.dev/). The following hyperparameters were optimized during training: input image size, encoder and decoder depth, kernel size, learning rate, batch size, kernel size and loss function. For the UNETR architecture, which in total had 92.8 million parameters, the best model based on DSC performance on the validation set had the following parameters: 12 attention heads, feature size of 16, input patch size of 96^3 voxels and batch size of 24. The U-Net architecture, which in total had 4.8 million parameters, had the following parameters: a five-layer encoder with an initial channel size of 16 and kernel size of 3 × 3 × 3, input patch size of 128^3 voxels and batch size of 27.

The UNETR and U-Net models were trained for 700 and 580 epochs, respectively. To avoid overfitting, early stopping was set to 50 epochs where performance (DSC) on the validation dataset did not improve. The Adam optimizer[76] was used with an initial learning rate of 0.0001.

Implementation

All DL models were implemented in Python using the Medical Open Network for Artificial Intelligence framework (MONAI[77]), and the PyTorch machine learning framework[78]. All training was performed on the Cedar and Narval cluster provided by the Digital Research Alliance of Canada (www.alliancecan.ca), using NVIDIA V100 Volta graphic processing units with 32 GB of memory, and A100 graphic processing units with 40 GB of memory. Registration of our data to ARA was performed with our in-house, open-source MIRACL[10] software. MIRACL is fully containerized and available as Docker and Singularity/Apptainer images (https://miracl.readthedocs.io/). For results visualization, we used a variety of open-source software applications and Python libraries, including matplotlib, seaborn, Brainrender[79], Fiji/ImageJ[38], itk-SNAP[80] and Freeview (http://surfer.nmr.mgh.harvard.edu/). We also used BioRender for figure creation in this manuscript (https://www.biorender.com/).

Data augmentation

To increase the generalizability of the DL model and model distribution shifts in LSFM data, the training set images were randomly augmented in real time at every epoch. Supplementary Fig. 3 shows all the data augmentation transforms used, namely: affine transformations, contrast adjustment, histogram shift, random axis flipping and different noise distributions such as salt and pepper, and Gaussian. These transforms were selected because they are representative of distortions that occur during LSFM imaging. Briefly, a range (0, 1) of scaling was applied to each 512^3-image patch, based on the intensity distribution of that patch. The intensity of each 512^3-image patch was scaled from the [0.05, 99.5] percentile to [0, 1], where 0.05 and 99.95 are the intensity values at the corresponding percentiles of the image patch. Subsequently, each data augmentation transform was randomly applied (with a probability of $P = 0.5$) to the 512^3-image patch at each epoch. The parameters of each data augmentation were also randomly selected at each epoch from the predetermined range of values.

Voxel-wise uncertainty map

Epistemic uncertainty, as described previously[35], is rooted in a lack of knowledge about model parameters and structure, rather than stemming from inherent variability in the observed data; this type of uncertainty is often referred to as model uncertainty[35]. To estimate the models' uncertainty and confidence in predictions, we used the Monte Carlo dropout approach. During training, dropout layers (with a probability of $P = 0.2$) were utilized as a regularization technique. It has been shown that turning on dropout layers (randomly switching neurons off) in inference mode can be interpreted as a Bayesian approximation of the Gaussian process[36]. At test time, when the dropout layers are turned on, each forward pass yields a stochastically different prediction as a sample from the approximate parametric posterior distribution ($P(y|X)$)[37]. This technique has been shown to provide useful insights into the model's uncertainty, by computing the variance of numerous predictions ($Y = \{y_1, y_2, \ldots, y_N\}$). Voxel-wise uncertainty (variance) can thus be defined[7]:

$$\text{Voxel-wise uncertainty} \simeq \frac{1}{N}\sum_{n=1}^{N}y_n^2 - \left(\frac{1}{N}\sum_{n=1}^{N}y_n\right)^2$$

The resulting voxel-wise uncertainty map provides a measure of variation in predictions of slightly different models for the same data, which can be particularly useful in identifying regions of high uncertainty.

Ensemble of ensembles

Each model's output was obtained by averaging the probability maps of 50 models ($Y = \{y_1, y_2, \dots, y_{50}\}$) using the Monte Carlo dropout technique:

$$\hat{Y}_{\text{Ensembles}} = \frac{1}{50}\sum_{i=1}^{50} y_i$$

Subsequently, to combine the prediction maps of both models, a final mapping of neurons was generated using an ensemble of both models (ensemble of ensembles):

$$\hat{Y}_{\text{Ensemble of ensembles}} = \frac{1}{2}\left(\hat{Y}_{\text{Ensembles}_{\text{U-Net}}} + \hat{Y}_{\text{Ensembles}_{\text{UNETR}}}\right).$$

Model evaluation

Evaluation metrics. To evaluate the performance of the segmentation models, several volume- and shape-based metrics were used, including DSC, recall, precision, $F1$ score and HD_{95}. We used the metrics derived from the resulting confusion matrix and associated true-positive (TP), FP and FN values. Each neuronal soma was defined as a 3D connected component. Given this definition, TP was defined as the number of correctly detected neurons following comparison of GT with prediction P. Sensitivity or recall measures the proportion of TP relative to the number of individual neurons delineated in GT, and was defined as

$$\text{Recall} = \frac{\text{TP}}{\text{TP} + \text{FN}}.$$

Precision measures the proportion of TP against all positive predictions, and was defined as

$$\text{Precision} = \frac{\text{TP}}{\text{TP} + \text{FP}}.$$

While recall is useful to gauge the number of FN pixels in an image, precision is useful to evaluate the number of FP pixels in a prediction.

The $F1$ score combines precision and recall, and is often used to measure the overall performance of a model. The $F1$ score measures the number of wrongly detected neurons in P:

$$F1\,\text{score} = \frac{2 \times \text{Precision} \times \text{Recall}}{\text{Precision} + \text{Recall}}.$$

DSC measures the number of elements common to GT and P datasets, divided by the sum of the elements in each dataset, and is defined as

$$\text{DSC}(\text{GT}, P) = 2 \times \frac{|\text{GT} \cap P|}{|\text{GT}| + |P|}.$$

Hausdorff distance is a mathematical measurement of the 'closeness' of two sets of points that are subsets of a metric space; it is the greatest of all distances from a point in one set to the closest point in the other. We used the 95th percentile of Hausdorff distance rather than the maximum results, to provide a more robust and representative measure of the segmentation's performance in image analysis tasks. Given two sets of points, X and Y, Hausdorff distance between these two sets was defined as

$$\text{HD}(X, Y) = \max\{\sup_{x\in X}\inf_{y\in Y} d(x,y), \sup_{y\in Y}\inf_{x\in X} d(x,y)\}.$$

Simulation distribution shift. We deployed our recently published ROOD-MR platform (https://github.com/AICONSlab/roodmri) on our test data, which includes methods for simulating distribution shifts in datasets at varying severity levels using imaging transforms and generating benchmarking segmentation algorithms based on robustness to distribution shifts and corruptions. We employed three commonly used transforms that disrupt low-level spatial information (Gaussian noise, smoothing and sharpening). We added Gaussian noise to the image with zero mean and $0 < \sigma < 1$. For sharpening, we used a Gaussian blur filter with a zero mean and $0.05 < \sigma < 2$. We also applied a Gaussian smooth filter to the input data based on the specified sigma (σ) parameter ($0.05 < \sigma < 2$).

Comparison against Ilastik. We used the pixel classification module in Ilastik and trained a RF classifier using all training subjects (18 whole-brain LSFM images). We used 37 three-dimensional filters and an RF classifier with 100 trees. To train the RF model, we randomly selected three 512^3-voxel image patches from each subject and applied the same scale-intensity transform (Supplementary Fig. 3) used in the DL training approach, to provide a fair comparison. Next, we dedicated around 2 h per image patch on a personal computer (with 24 central processing unit cores and 512 GB memory) for annotating neurons and providing feedback to the RF algorithm, to achieve optimal results. Finally, the trained RF classifier was used to generate segmentation maps for all test and unseen datasets. For quantitativel evaluation of ACE robustness across different regions of the brain, we registered the test set to ARA 10 µm, warped ARA labels back to their native space and integrated warped labels with segmentation maps.

Comparison against Cellfinder. We used Cellfinder to generate whole-brain detection maps of neuronal cell bodies. We first used their pretrained Resnet model to generate detection maps on both test and unseen datasets. We deployed the Cellfinder command with −no-registration flag to detect and classify cells to either background or neuron. For retraining Cellfinder, we randomly selected two subjects from the test set and generated ~6,100 (~3,200 cells and ~2,900 non-cells) annotated cell candidates for the first subject and ~9,000 (~4,300 cells and ~4,700 non-cells) for the second subject, using their Napari-cellfinder plugin. The training data were then used to retrain the Resnet model by incorporating the function cellfinder_train and the flag −continue-training, keeping other options as default. Lastly, the best retrained model based on validation error was used to generate whole-brain detection maps. For quantitative comparison against Cellfinder, we transformed ACE segmentation maps into detection maps by finding the center of mass of each neuron in 3D.

Voxelization, registration and heatmap generation

Voxelization. To synthesize and correlate our segmentation results within the ARA space, a voxelization process was used. Voxelization entailed the transformation of high-resolution segmentation outcomes into a 10-µm resolution space while minimizing loss of information. Segmentation volumes underwent convolution with a spherical kernel featuring a radius of ~5 µm—a dimension that aligns with the downsampling factor and ARA space. Subsequently, within each convolved sphere, the average count of labels (cells or nuclei) was computed, resulting in a voxelized map. This 3D voxelized representation, which was generated using Python's skimage library with parallel computation facilitated by the joblib and multiprocessing libraries, allowed for efficient feature extraction summarized by ARA regions/labels.

Registration. To bring whole-brain tissue-cleared microscopy images, segmentation maps and a reference atlas (ARA) into spatial correspondence, we used our open-source MIRACL[10] platform. MIRACL contains specialized workflows that are optimized for multimodal registration of cleared data, based on tools from ANTs[81] (http://stnava.github.io/ANTs/). Registration workflows include a cascade of image-preprocessing techniques, such as denoising and intensity correction, as well as an intensity-based alignment[40]. The alignment process consists of two main steps. In the first of these, an initial alignment is carried out using the antsAffineInitializer tool from ANTs[81]; the second step consists of an intensity-based, multistage, b-spline registration algorithm encompassing a rigid six degrees of freedom, an affine (12 degrees of freedom) and a nonrigid (deformable) b-spline symmetric normalization stage. The rigid and affine stages are based on maximization of the mutual information similarity metric between ARA and microscopy data, while the deformable stage uses cross-correlation as the similarity metric. The resulting transformations perform bidirectional warping of images to and from tissue-cleared microscopy native space and ARA space.

Heatmap generation. Voxelized segmentation maps were warped to the ARA space (10-µm resolution) using a deformation field obtained through registration. Subsequently, a smoothing Gaussian filter was applied with a sigma of four pixels. Difference heatmaps were then computed by subtracting the average of voxelized and warped segmentation maps in each group.

ROI-based analysis

We passed the voxelized and warped segmentation map at a resolution of 10 µm, in addition to the registered labels for each subject, to MIRACL's function seg feat_extract, to extract the density of cells per ARA region for both the whole brain and labels grouped to a maximum atlas ontology depth of 6. The ARA labels are structured into descending depth, from coarse- to fine-grained groupings of brain regions, with MIRACL's function combining labels at a higher depth by their parent labels. The resulting density results were then passed to MIRACL's function group_unpaired_ttest, which applied Student's paired t-test (two-sided) per label with an alpha value of 0.05 for both whole-brain regions and depth 6 regions, and both applications. This function creates bar plots that compare the density of cells per ARA label, including both significant ROIs and trending regions ($P < 0.1$). Lastly, MIRACL's function proj_stats_on_atlas was used to project the resulting P values on the atlas regions.

Cluster-wise, permutation-based statistical algorithm and analysis

We developed a cluster-wise, permutation-based statistical algorithm with TFCE. The statistical pipeline consisted of three main steps, and is based on the implementation of the function spatio_temporal_cluster_test from MNE (https://mne.tools/stable/index.html). In the first step, a voxel-wise statistical test using two-way ANOVA was performed between two groups of study. To incorporate the correlation structure of the data and correct for multiple comparisons, we considered a null hypothesis regarding the sizes of clusters in our data rather than focusing on individual voxels. Thus, in the second step, clusters were defined using adjacency structure in our data (connecting each voxel to its neighbors in 3D) and the TFCE technique[44], which addresses the challenge of selecting a threshold for both cluster-forming and smoothing problems. We optimized the adjacency structure of the data using a priori knowledge from group-wise heatmaps to boost the sensitivity of the statistical results in teravoxel LSFM data, due to the exceedingly large number of voxels (and hence the number of statistical tests). Specifically, the adjacency matrix was masked using a thresholded (90% percentile) and then dilated version of the group-difference heatmap, allowing the algorithm to focus only on putative clusters. TFCE transforms a raw statistical image into a map that reflects the strength of local spatial clustering. The new value assigned to each voxel is determined by aggregating the scores of all supporting sections below it. The score of each section is computed by taking the height of the section (raised to a power H) and multiplying it by the extent of the section (raised to a power E):

$$\mathrm{TFCE}(v) = \int_{h=h_0}^{h_v} e(h)^E h^H \mathrm{d}h,$$

where h_0 is typically around zero and h_v is a statistic value corresponding to voxel v. In practice, this integral is estimated as a sum, using finite step sizes ($\mathrm{d}h$). The exponents of the powers (E and H) are free parameters, but fixing these values has been shown to yield robust outcomes justified by theory and empirical results[44,59]. Increasing H gives more weight to clusters with higher effect size, while increasing E gives more weight to larger clusters[44]. In our analysis we chose $E = 2$, $H = 0.5$, $h_0 = 0$ and a step size of 5 to mitigate the potential impact of FP in LSFM data, and fixed the values for both applications, walking and food-seeking datasets. The application of TFCE transforms results in a weighted sum of local cluster-like signals, eliminating the need for a fixed threshold to define clusters while keeping the local minima and maxima at the same spot. The size of each cluster was measured by the sum of voxels' F-values within the cluster. In the final step, a nonparametric permutation test ($N = 1,000$) was applied and new cluster-wise F-statistics were obtained. In each permutation, the same procedure was applied to define clusters and compute their statistics, with the largest cluster size being retained. We also used the stepdown P value procedure to boost sensitivity while controlling for family-wise error rate[82]. To test the significance of clusters in our actual data, a null distribution was obtained via permutations. Cluster sizes observed in the actual data are compared with those in the null distribution to calculate P values, which can then be compared with a predetermined threshold (such as alpha <0.05 or false-detection rate-corrected P values) to test for significance. Next, we applied connected component analysis on the resulting P value image to summarize significant clusters. Finally, by integration of connected component analysis results, ARA labels and density heatmaps, we extracted the center, mean effect size and volume of each cluster, along with the percentage volume within each brain region spanned.

Cluster-wise connectivity analysis

The significant clusters identified through ACE's cluster-wise, permutation-based statistical algorithm were systematically ranked based on their statistical effect size and volume. To streamline the subsequent connectivity analysis, we selected the top 20 clusters from this ordered list. Integrating each cluster's location with voxelized and warped segmentation maps, we calculated the mean intensity of each cluster per subject in both treated and control groups. Subsequently we employed a Pearson correlation test, utilizing the function pearsonr from the scipy library, between the mean intensity values of each pair of clusters. For each correlation coefficient, we established an 80% confidence interval using the bias-corrected and accelerated bootstrap method with 10,000 iterations, and selected the lower bound. Finally, the P value associated with each correlation test was determined through permutation testing, involving 10,000 permutations. For visualization, significant correlation coefficients ($P < 0.01$) were plotted alongside a heatmap illustrating Euclidean distance between each pair of cluster centroids.

Native space cluster validation

The significant clusters identified through ACE's cluster-wise TFCE permutation-based statistical algorithm were binarized using $\sigma = 0.05$ (or a user-fed threshold). Next, binarized clusters underwent a dilation (one iteration, using binary_dilation from the scipy.ndimage package) and a connected component analysis (using label function from the scipy.ndimage package) to differentiate each cluster. Processed significant clusters were then warped to the native space of each subject using registration transformations and the function miracl lbls warp_clar. Utilizing ACE segmentation maps, the number of neurons within each cluster was computed by identifying the coordinates of each neuron. A two-sided Mann–Whitney *U*-test (from the scipy.stats package) was deployed to compare the number of neurons within each cluster across two groups. The numbers of neurons per subject for each cluster—in addition to their volume, atlas space *P* value and cluster-wise statistics (obtained by ACE cluster-wise TFCE permutation), percentage volume within each overlapping brain region and native space *P* value (obtained by post hoc Mann–Whitney *U*-test)—are summarized in a comma-separated values file.

Reporting summary

Further information on research design is available in the Nature Portfolio Reporting Summary linked to this article.

Data availability

A subset of the datasets (whole-brain LSFM data and voxelized and warped segmentation maps) generated and analyzed during the current study are available at https://miracl.readthedocs.io/, within an ACE workflow tutorial (https://miracl.readthedocs.io/en/latest/tutorials/workflows/ace_flow/ace_flow.html), as examples with the pipeline. All required files, including the ARA, labels and datasets, are included in the MIRACL containers with documentation and tutorials.

Code availability

We have made our ACE pipeline publicly available to the research community as an end-to-end module within our open-source MIRACL platform (under license no. GPL-3.0) at https://miracl.readthedocs.io/, along with documentation, tutorials, example data, graphical user interfaces and visualization functions. ACE is implemented in a modular fashion with many well-documented core modules (functions) that can be executed as command-line tools or accessed through MIRACL graphical user interfaces (Supplementary Fig. 5), including segmentation (trained DL models with easy-to-use, fine-tuning scripts), voxelization, registration and statistical analysis.

References

61. Takeoka, A., Vollenweider, I., Courtine, G. & Arber, S. Muscle spindle feedback directs locomotor recovery and circuit reorganization after spinal cord injury. *Cell* **159**, 1626–1639 (2014).
62. Yun, D. H. et al. Ultrafast immunostaining of organ-scale tissues for scalable proteomic phenotyping. Preprint at https://www.biorxiv.org/content/10.1101/660373v1 (2019).
63. Murray, E. et al. Simple, scalable proteomic imaging for high-dimensional profiling of intact systems. *Cell* **163**, 1500–1514 (2015).
64. Tomer, R., Ye, L., Hsueh, B. & Deisseroth, K. Advanced CLARITY for rapid and high-resolution imaging of intact tissues. *Nat. Protoc.* **9**, 1682–1697 (2014).
65. Bria, A. & Iannello, G. TeraStitcher – a tool for fast automatic 3D-stitching of teravoxel-sized microscopy images. *BMC Bioinformatics* **13**, 316 (2012).
66. Wagner, T. & Lipinski, H.-G. IJBlob: an ImageJ library for connected component analysis and shape analysis. *J. Open Res. Softw.* **1**, e6 (2013).
67. Vuola, A. O., Akram, S. U. & Kannala, J. Mask-RCNN and U-Net ensembled for nuclei segmentation. In *2019 IEEE 16th International Symposium on Biomedical Imaging (ISBI 2019)* 208–212 (IEEE, 2019); https://doi.org/10.1109/ISBI.2019.8759574
68. Hatamizadeh, A. et al. UNETR: transformers for 3D medical image segmentation. Preprint at https://arxiv.org/abs/2103.10504 (2021).
69. He, K., Zhang, X., Ren, S. & Sun, J. Deep residual learning for image recognition. In *2016 IEEE Conference on Computer Vision and Pattern Recognition (CVPR)* 770–778 (IEEE, 2016); https://ieeexplore.ieee.org/document/7780459
70. Kerfoot, E. et al. In *Statistical Atlases and Computational Models of the Heart. Atrial Segmentation and LV Quantification Challenges* (eds Pop, M. et al.) 371–380 (Springer International Publishing, 2019); https://doi.org/10.1007/978-3-030-12029-0_40
71. Ronneberger, O., Fischer, P. & Brox, T. in *Medical Image Computing and Computer-Assisted Intervention – MICCAI 2015* (eds Navab, N. et al.) 234–241 (Springer International Publishing, 2015).
72. Falk, T. et al. U-Net: deep learning for cell counting, detection, and morphometry. *Nat. Methods* **16**, 67–70 (2019).
73. He, K., Zhang, X., Ren, S. & Sun, J. Delving deep into rectifiers: surpassing human-level performance on ImageNet classification. Preprint at https://doi.org/10.48550/arXiv.1502.01852 (2015).
74. Ioffe, S. & Szegedy, C. Batch normalization: accelerating deep network training by reducing internal covariate shift. Preprint at https://arxiv.org/abs/1502.03167 (2015).
75. Srivastava, N., Hinton, G., Krizhevsky, A., Sutskever, I. & Salakhutdinov, R. Dropout: a simple way to prevent neural networks from overfitting. *J. Mach. Learn. Res.* **15**, 1929–1958 (2014).
76. Kingma, D. P. & Ba, J. Adam: a method for stochastic optimization. Preprint at https://arxiv.org/abs/1412.6980 (2017).
77. Cardoso, M. J. et al. MONAI: an open-source framework for deep learning in healthcare. Preprint at https://doi.org/10.48550/arXiv.2211.02701 (2022).
78. Paszke, A. et al. PyTorch: an imperative style, high-performance deep learning library. Preprint at https://doi.org/10.48550/arXiv.1912.01703 (2019).
79. Claudi, F. et al. Visualizing anatomically registered data with brainrender. *eLife* **10**, e65751 (2021).
80. Yushkevich, P. A. et al. User-guided 3D active contour segmentation of anatomical structures: significantly improved efficiency and reliability. *NeuroImage* **31**, 1116–1128 (2006).
81. Avants, B. B. et al. A reproducible evaluation of ANTs similarity metric performance in brain image registration. *NeuroImage* **54**, 2033–2044 (2011).
82. van der Laan, M., Dudoit, S. & Pollard, K. Multiple testing. Part II. Step-down procedures for control of the family-wise error rate. *Stat. Appl. Genet. Mol. Biol.* **3**, 14 (2004).

Acknowledgements

This work was supported by funding from the Canadian Institute of Health Research (grant nos. PJT178059, PJT376309 and PJT156179), the Natural Sciences and Engineering Research Council (discovery grant no. RGPIN-2021-03728) and the Alzheimer's Society (young investigator grant no. 23-05). A.A. was funded by the Department of Medical Biophysics, University of Toronto's Excellence Award. B.S. is funded by the Canada Research Chairs program (award no. CRC-2018-00042). M.G. is funded by the Canada Research Chairs program (award no. CRC-2021-00374). We thank the Digital Research Alliance of Canada (alliancecan.ca) for their allocation of computing resources used in parts of this research. We are grateful for support from the Black Centre for Brain Resilience and Recovery and the Harquail Centre for Neuromodulation. We thank Z. Pang and members of the Ye laboratory at the Scripps Research Institute for sharing fine-tuning imaging data. We also thank J. Tan and E. Pineau, members of the AICONS and functional brain-imaging laboratories at the University of Toronto, for useful discussions about accessibility of the manuscript and pipeline.

Author contributions

A.A., B.S. and M.G. conceived and led the development of ACE. A.A. developed and evaluated all DL models, conducted all data processing and statistical analysis and created the figures, with input from M.G. and B.S. A.A. and M.G. designed and optimized the cluster-wise analysis for LSFM data. T.Q., N.L., L.Y., N.C., J.S. and G.C. contributed to the collection of data and interpretation of results. M. Raffiee, M. Rozak, K.D., and J.M. contributed to the experimental

design and interpretation of results. J.O. contributed to image registration and ROI-based statistical analysis. J.O., A.R., A.A. and M.G. developed and implemented the ACE Docker and integration with the MIRACL platform. S.P. and F.Y. assisted with GT data generation and DL model development. A.A., B.S. and M.G. wrote the manuscript, with input from all coauthors. M.G. and B.S. received funding and supervised all aspects of this work.

Competing interests

The authors declare no competing interests.

Additional information

Extended data is available for this paper at https://doi.org/10.1038/s41592-024-02583-1.

Supplementary information The online version contains supplementary material available at https://doi.org/10.1038/s41592-024-02583-1.

Correspondence and requests for materials should be addressed to Maged Goubran.

Peer review information *Nature Methods* thanks the anonymous reviewers for their contribution to the peer review of this work. Peer reviewer reports are available. Primary Handling Editor: Nina Vogt, in collaboration with the *Nature Methods* team.

Reprints and permissions information is available at www.nature.com/reprints.

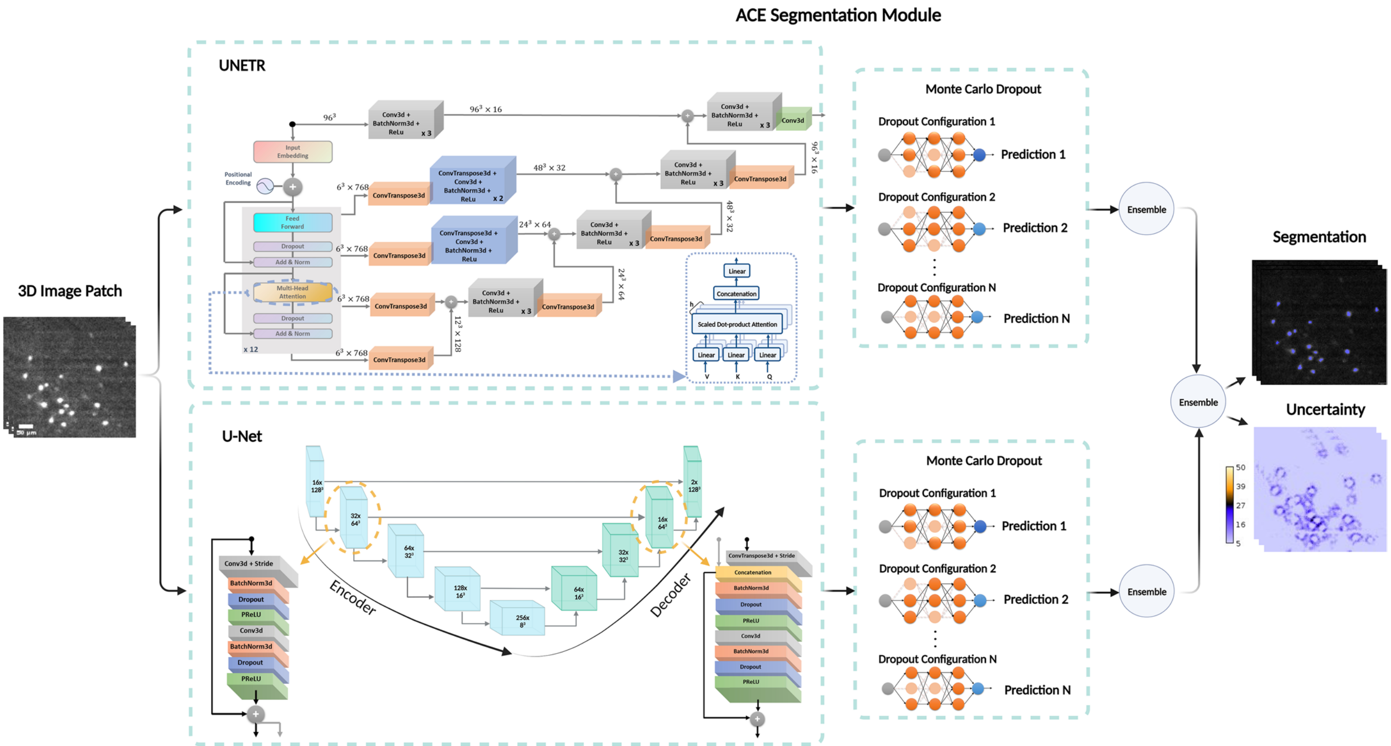

Extended Data Fig. 1 | ACE's segmentation module. A 3D vision transformer (UNETR) with multi-head attention was used as our backbone architecture. Our optimized UNETR model receives an 96^3 image patch and generates a probability map of the same size. ACE also consists of a convolutional neural network-based 3D U-Net architecture, operating on 128^3 image patches. The probability map of each model is passed to a Monte-Carlo dropout block to estimate model confidence and generate an ensemble of 50 models, improving the accuracy of the overall prediction. To increase the generalizability of the ACE segmentation module, the user can deploy another layer of ensembling by combining both UNETR and U-Net outputs. Created in BioRender.com.

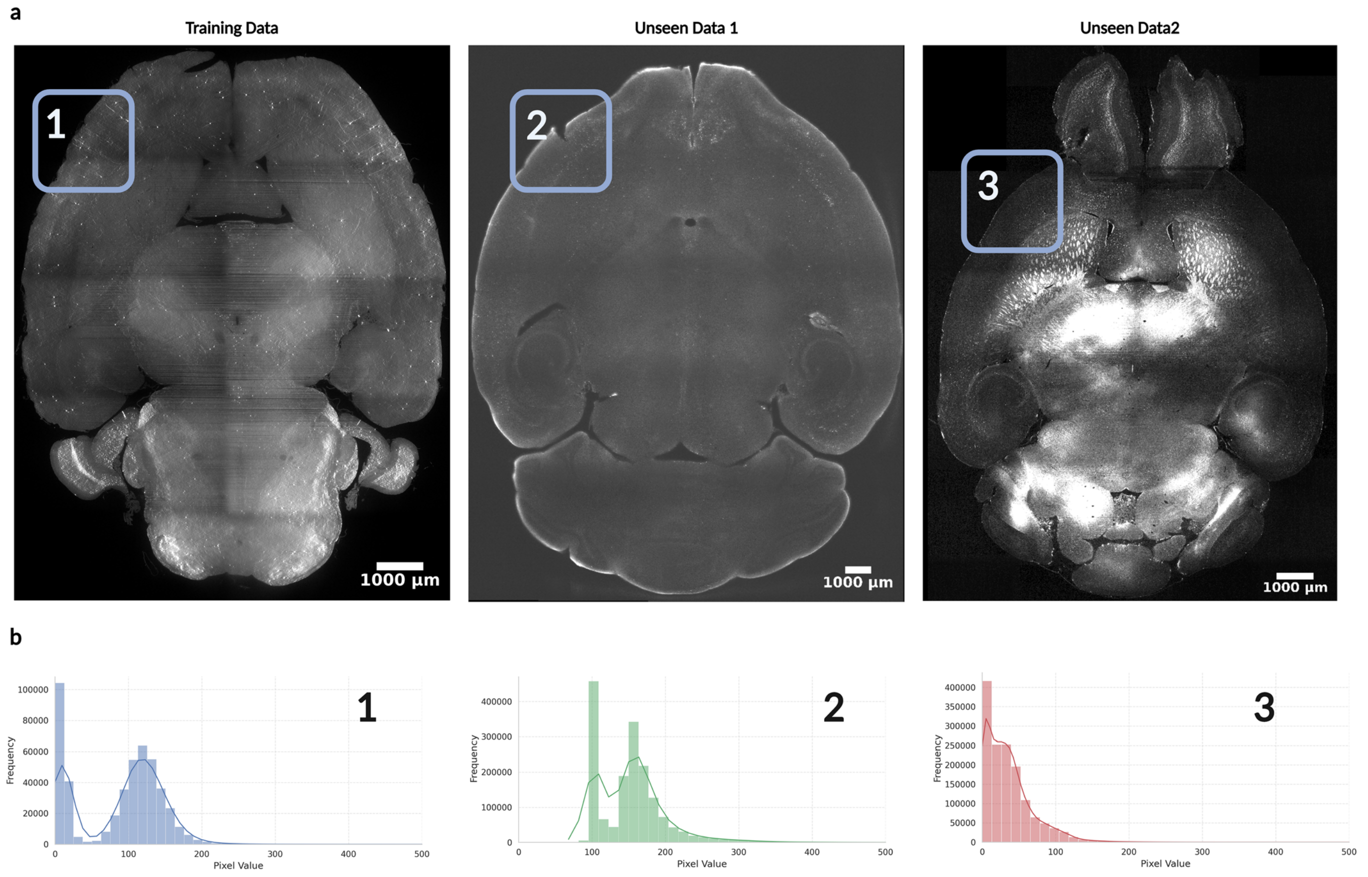

c

	Microscope	Tissue Clearing	Voxel Size (µm)	Fluorophore	SNR (db)	CNR (db)
Training Data	SmartSPIM	SHIELD	3.5x3.5x4	tdTomato	10.8 ± 1.0	11.1 ± 2.2
Unseen Data 1	COLM	iDISCO	1.4x1.4x5	Alexa Fluor 647	2.1 ± 0.4	8.1 ± 1.3
Unseen Data 2	SmartSPIM	SHIELD	1.8x1.8x4	Alexa Fluor 647	7.8 ± 2.0	7.7 ± 0.8

Extended Data Fig. 2 | Light-sheet fluorescence microscopy (LSFM) datasets used to develop and evaluate ACE's deep learning models. Our training data consists of 18 animals with 10 acquired from the whole brain and eight animals with data acquired from the left hemisphere. We used whole-brain LSFM datasets (see Methods-Datasets and Experiments) from different studies to evaluate ACE deep learning models. Panel **a** shows axial views of an example subject from each group. Panel **b** shows the intensity histogram of a randomly selected image patch for each subject shown in panel **a**. **c**. Image characteristics of each dataset. Our unseen datasets were obtained using a different experimental setup including a different microscope, rodent model, fluorescence proteins, and tissue-clearing technique. See Method–Datasets and Experiments for more details.

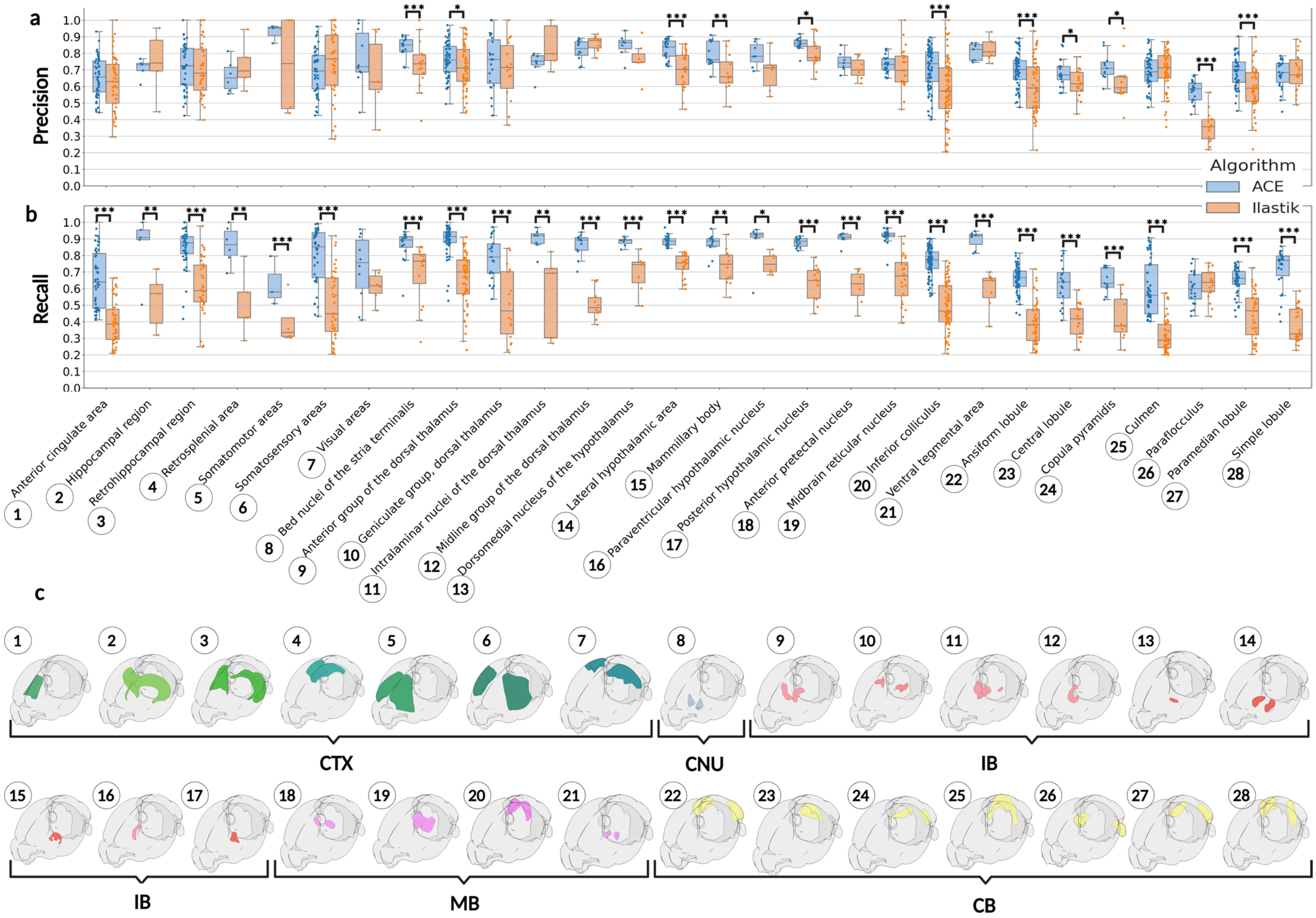

Extended Data Fig. 3 | ROI-wise evaluation of ACE segmentation module in segmenting neuronal cell bodies across the whole brain. Average precision **(a)** and recall **(b)** obtained between ACE outputs and ground truth per ARA label **(c)** and compared against Ilastik. In total N: 1600 unique patches with $96^3 \simeq 0.35\ mm^3$; minimum 10 and maximum 155 unique patches/region. Box plots: box limits, upper and lower quartiles; center line, median; whiskers, 1.5× interquartile range; points, outliers. Mann-Whitney U test (two-sided), ***P < 0.001, **P < 0.01, and ***P < 0.05.

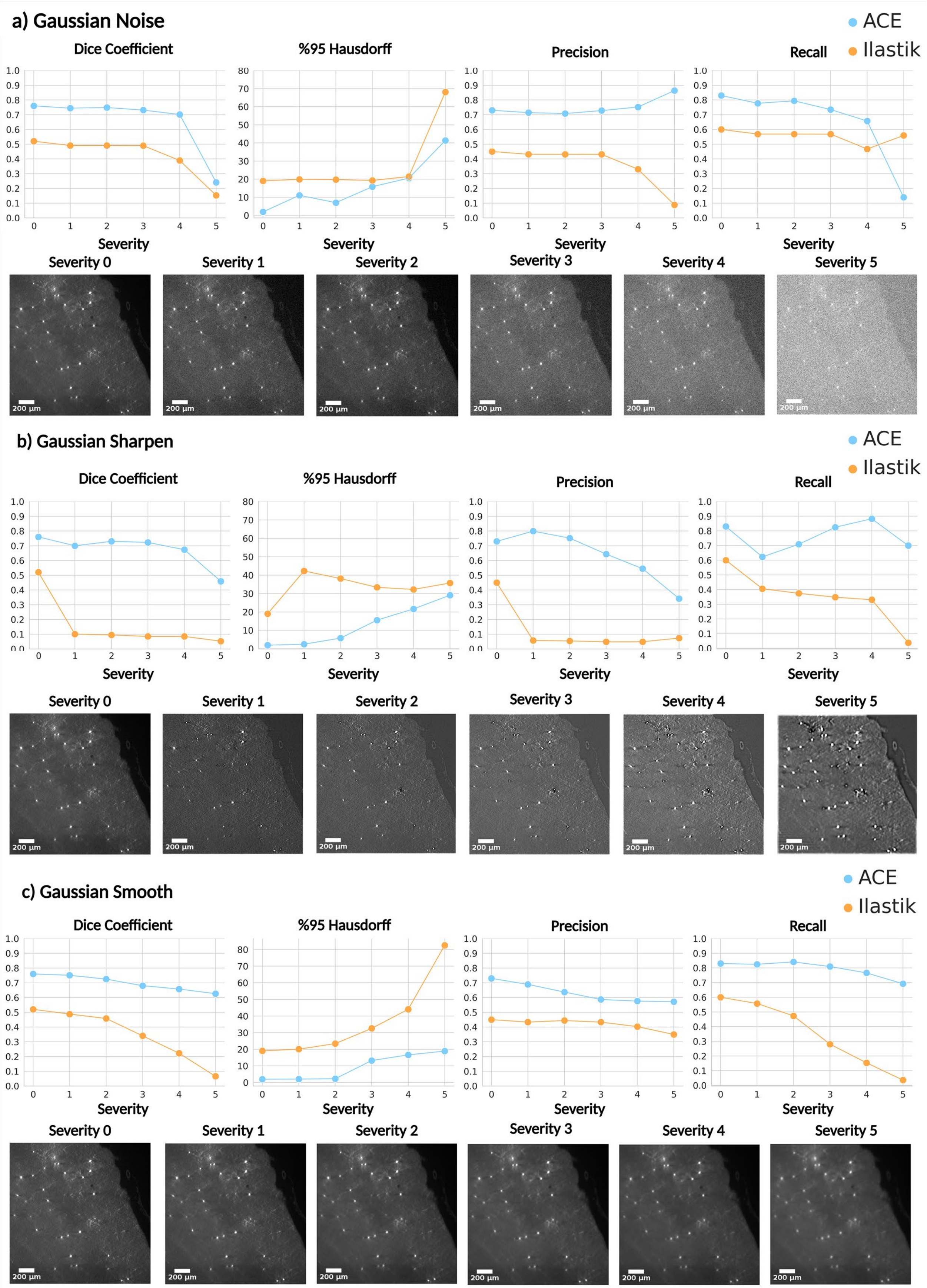

Extended Data Fig. 4 | Evaluation of ACE segmentation models' robustness to simulating distribution shifts. The x-axis of the first row in panels **a-c** shows the severity of each transform. The second row in each panel demonstrates the effect of each transform on the input image. **a**. Adding Gaussian noise to the image with zero mean and $0 < \sigma < 1$. **b**. Sharpening the image using the Gaussian Blur filter with zero mean and $0.05 < \sigma < 2$. **c**. Apply Gaussian smooth to the input data based on the specified parameter ($0.05 < \sigma < 2$).

https://doi.org/10.1038/s41592-024-02583-1

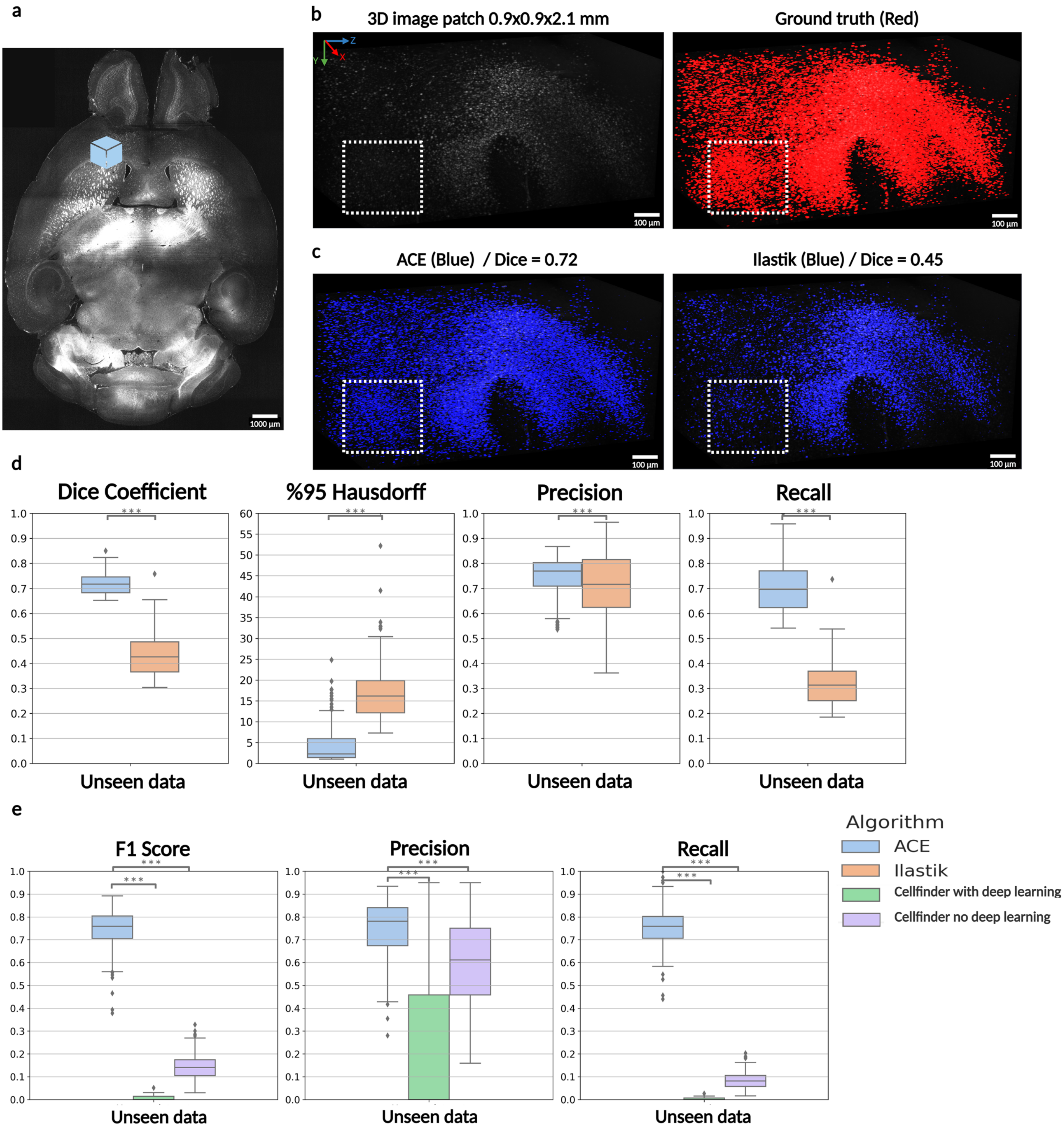

Extended Data Fig. 5 | Performance of ACE in brain-wide segmentation of neuronal cell bodies in unseen dataset 2. a. An axial view from a random depth of whole-brain c-Fos expression with an enlarged view of a cortical patch plus its associated ground truth data in red (**b**). **c**. The segmentation maps (blue) predicted by the ACE UNETR ensemble for the enlarged subregion are shown and compared with the Ilastik output for the same patch (blue). **d** and **e**. Quantitative evaluation of the segmentation accuracy of ACE vs. Ilastik (**d**) and detection accuracy of ACE vs. Cellfinder (**e**) in terms of average Dice coefficient, precision, recall, 95% Hausdorff distance, and F1 score on (N: 152 unique patches of 963≃0.17×0.17×0.38 mm^3). Box plots: box limits, upper and lower quartiles; center line, median; whiskers, 1.5× interquartile range; points, outliers. Mann-Whitney U test (two-sided), ***p < 0.0001.

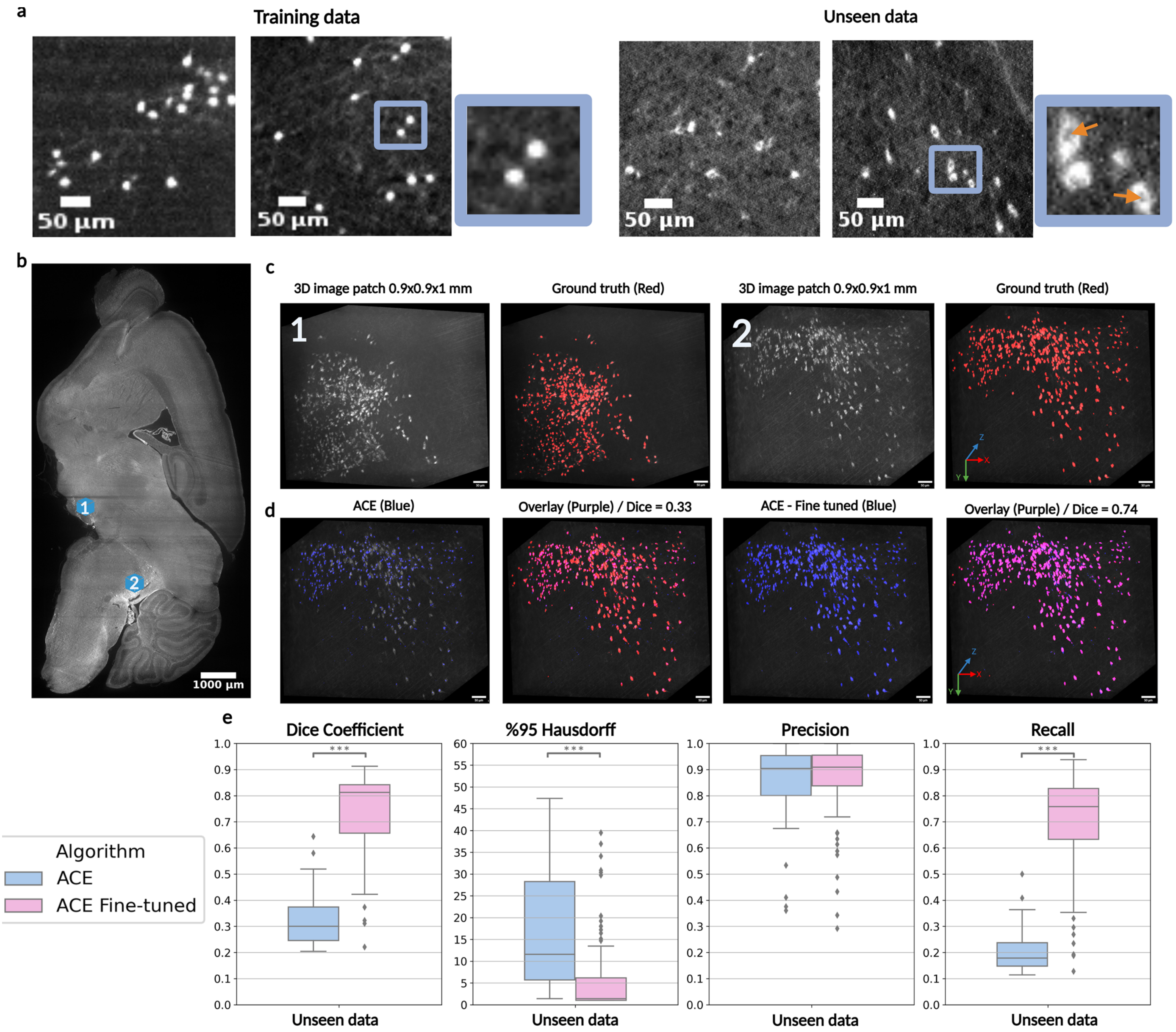

Extended Data Fig. 6 | Fine-tuning ACE segmentation models to segment other cellular markers with different morphological features compared to c-Fos. Panel **a** shows a randomly selected image patch from training data vs. a new unseen dataset with an enlarged view of several cells to highlight the different morphological appearance. **b**. An axial view from a random depth of the whole brain of the new dataset. **c**. two randomly selected image patches (with the size of 512x512x512 voxels); patch number 1 was used to fine-tune the ACE UNETR model while patch number 2 was used to evaluate the model performance. **d**. Qualitative ACE performance before and after fine-tuning. **e**. Quantitative performance of ACE deep learning models on N: 152 unique patches of 963≃0.17×0.17×0.19 mm3. Box plots: box limits, upper and lower quartiles; center line, median; whiskers, 1.5× interquartile range; points, outliers. Mann-Whitney U test (two-sided), ***p < 0.0001.

https://doi.org/10.1038/s41592-024-02583-1

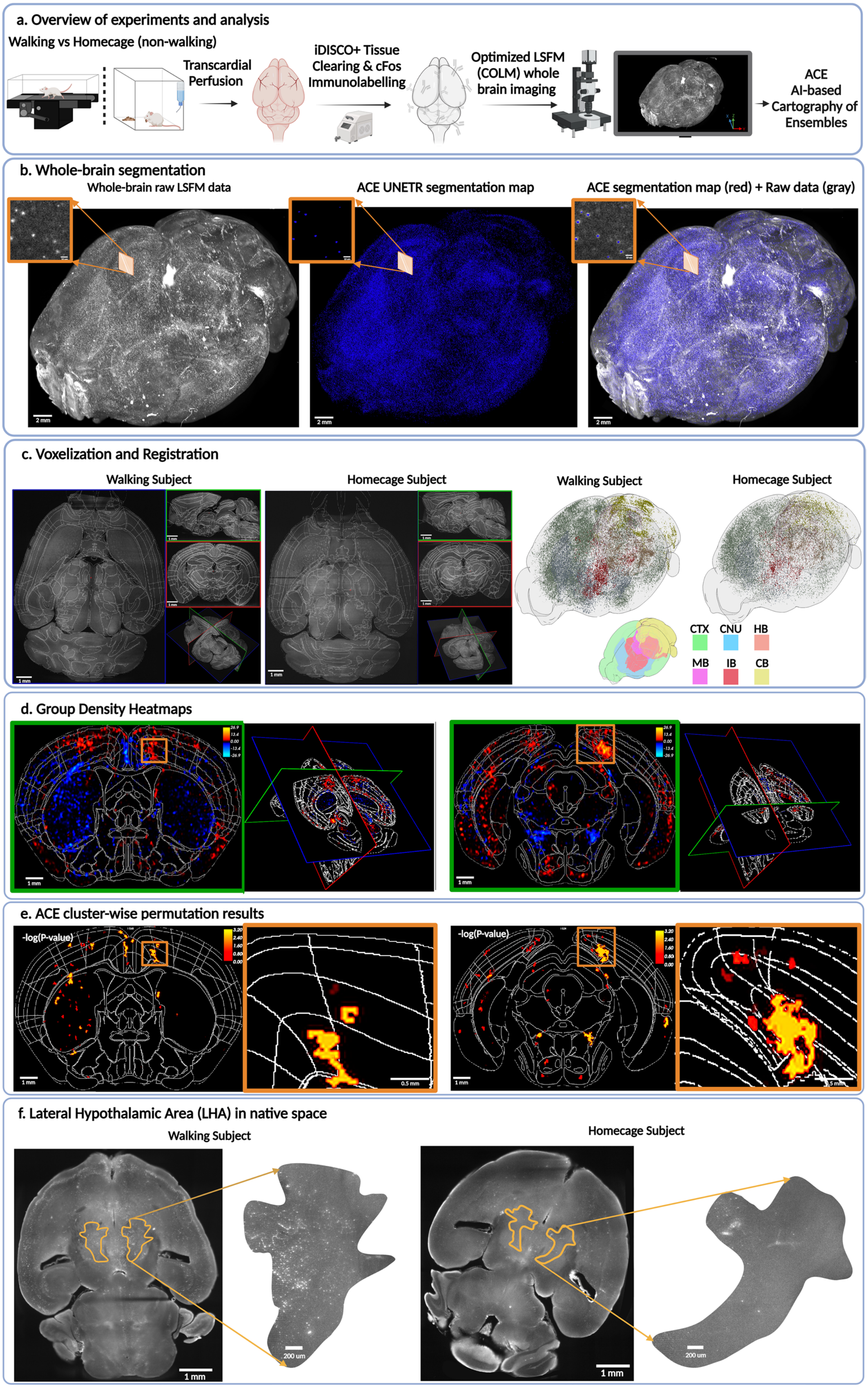
a. Overview of experiments and analysis
Walking vs Homecage (non-walking)
Transcardial Perfusion
iDISCO+ Tissue Clearing & cFos Immunolabelling
Optimized LSFM (COLM) whole brain imaging
ACE AI-based Cartography of Ensembles
b. Whole-brain segmentation
Whole-brain raw LSFM data
ACE UNETR segmentation map
ACE segmentation map (red) + Raw data (gray)
2 mm
c. Voxelization and Registration
Walking Subject
Homecage Subject
Walking Subject
Homecage Subject
1 mm
CTX
CNU
HB
MB
IB
CB
d. Group Density Heatmaps
1 mm
e. ACE cluster-wise permutation results
-log(P-value)
1 mm
0.5 mm
f. Lateral Hypothalamic Area (LHA) in native space
Walking Subject
Homecage Subject
1 mm
200 um

Extended Data Fig. 7 | See next page for caption.

Extended Data Fig. 7 | Brain-wide identification of local neuronal activity changes underlying walking. a. The overview of experimental design to analyze c-Fos+ cell distribution in whole-brain LSFM data during walking (n = 3/group). **b**. Automated segmentation of c-Fos+ cell distribution using ACE's segmentation module. Panels show a 3D rendering of a maximum intensity projection of raw data from the walking group, ACE output (blue), and raw data overlaid on ACE's output. **c**. Segmentation maps were voxelized to the ARA 10um resolution. Subsequently, the voxelized segmentation maps were warped to ARA space. Left panels show an example of a downsampled subject overlaid on ARA labels after registration from each group. Right panels show a 3D rendering of voxelized and warped segmentation maps color-coded based on 6 ARA regions: CTX, Cerebral Cortex; CNU, Cerebral Nuclei; MB, Midbrain; HB, Hindbrain; IB, Interbrain; and CB, Cerebellum. **d**. To identify neural activity hotspots, group-wise heatmaps of neuronal density were obtained by subtracting the average of the voxelized and warped segmentation maps in each group. Panels show two different coronal views as an example. **e**. Result of ACE cluster-wise threshold-free cluster enhancement permutation analysis, using a group-wise two-way ANOVA. The panels demonstrate the resulting p-value map representing the clusters showing significant differences between groups and corresponding to the coronal sections in **d**. Zoomed views show two significant clusters in MOp (left panel) and Retrosplenial area (right panel). See Supplementary Table 3 for strength (effect size), volume, and brain regions each cluster spanned. **f**. Lateral Hypothalamic Area (LHA) label was warped back into native space using the deformation matrix obtained by registration. Left and right panels show two example subjects from the walking and homecage groups respectively with a zoomed version of LHA, showcasing higher c-Fos+ activity in the walking vs. homecage condition. Section **a** is created in BioRender.com.

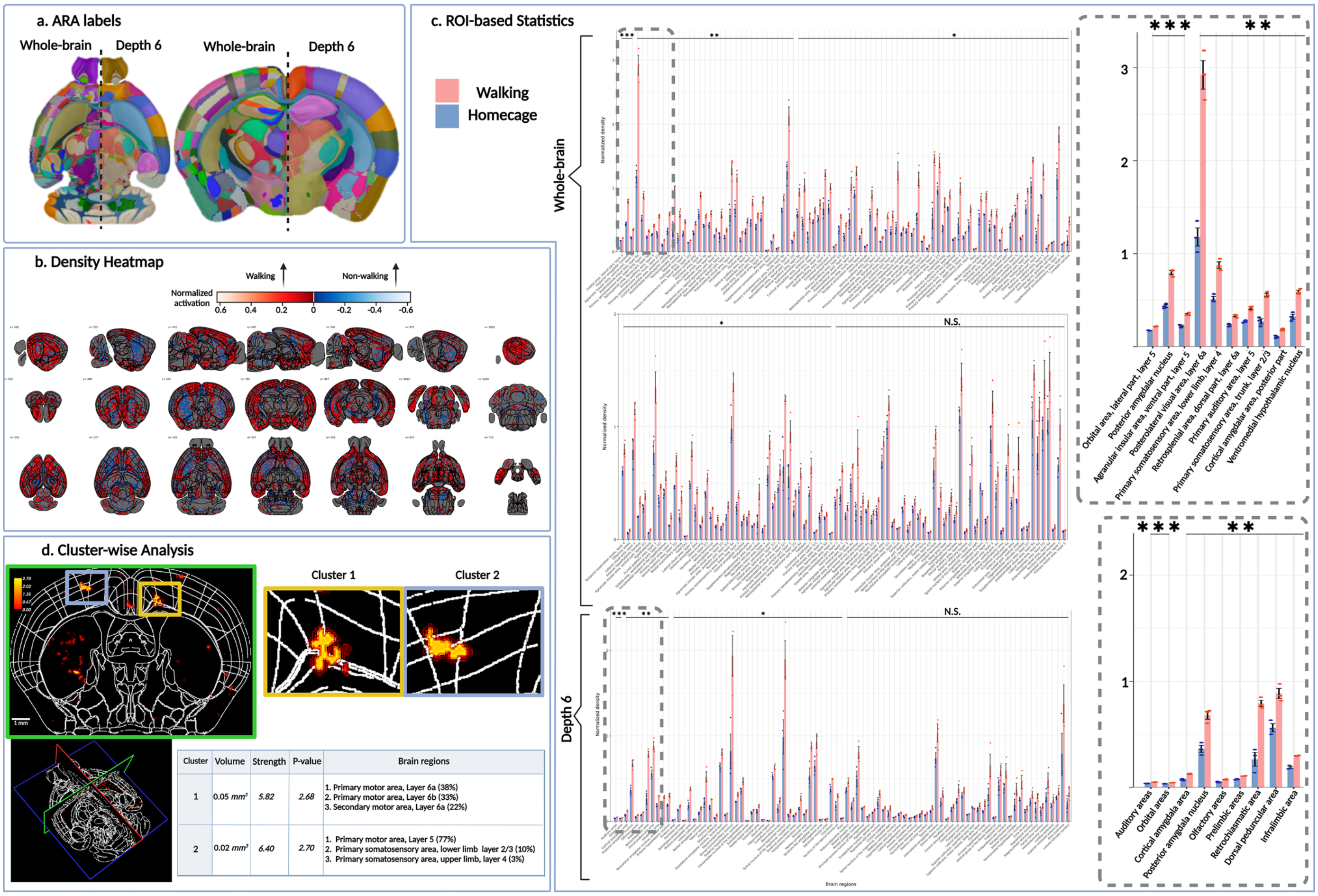

Cluster	Volume	Strength	P-value	Brain regions
1	0.05 *mm³*	*5.82*	*2.68*	1. Primary motor area, Layer 6a (38%) 2. Primary motor area, Layer 6b (33%) 3. Secondary motor area, Layer 6a (22%)
2	0.02 *mm³*	*6.40*	*2.70*	1. Primary motor area, Layer 5 (77%) 2. Primary somatosensory area, lower limb layer 2/3 (10%) 3. Primary somatosensory area, upper limb, layer 4 (3%)

Extended Data Fig. 8 | ACE statistical analysis for unraveling neuronal ensembles controlling walking. a. ARA labels at the level of whole brain vs. depth 6 based on the ARA ontology (hierarchy). **b**. Group-wise heatmaps of neuronal density were obtained by subtracting the average of the voxelized and warped segmentation maps in each group. Panels show different coronal, sagittal, and axial views as an example. **c**. Using voxelized and warped segmentation maps and ARA labels at 10 µm, we obtained neuronal density per brain region at both whole-brain and depth 6 levels. An independent student *t-test* (two-sided) was then applied between c-Fos+ cell density per ARA label to perform a whole-brain and depth 6 level ROI-wise statistical test (N: 3/group) Data are presented as mean values ± standard deviation. The upper panel shows the results of the whole-brain analysis with a zoomed version on the right, demonstrating the most significant ROIs. The lower panel shows the results of the depth 6 analysis. The ARA labels are sorted based on *p value* (***p < 0.001, **p < 0.01, and *p < 0.05). **d**. ACE cluster-wise analysis with group-wise two-way ANOVA documented several sub-regional and laminar neuronal clusters differentially activated during walking. Left panel shows a coronal view of a cluster-wise p-*value* map with two zoomed views of significant clusters spanning in the primary and secondary motor area layers 6, 6a and 6b and the primary somatosensory area layers 2/3 and 4. The table summarizes the information of each cluster. Using ACE cluster-wise analysis, the volume (µm3 x1,000^2), maximum strength (Cluster-wise TFCE F-statistic x1,000), brain regions each cluster spanned out on, and centroid of each significant cluster on Allen 10 µm atlas was computed.

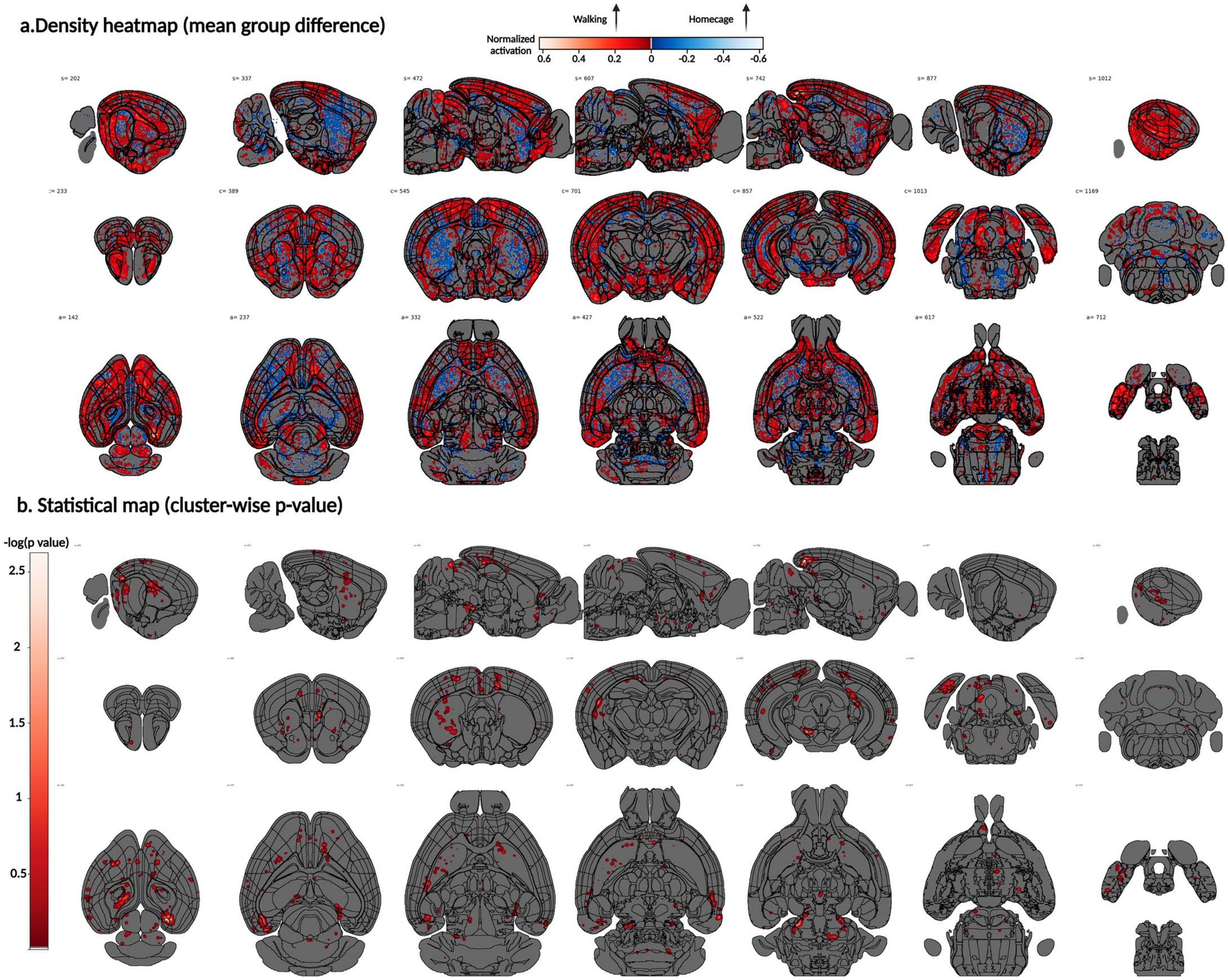

Extended Data Fig. 9 | ACE cluster-wise statistical analysis for unraveling neuronal ensembles controlling walking. a. Voxelized and warped segmentation maps, obtained by integrating ACE's segmentation module and MIRACL registration algorithms, were averaged per group. The average of the homecage (non-walking) group was subtracted from the walking group to obtain a density heatmap, demonstrating neuronal hotspots differentially activated in the walking group. **b**. Statistical whole-brain *p-value* map obtained by ACE cluster-wise analysis with a group-wise two-way ANOVA, demonstrating several sub-regional and laminar neuronal clusters differentially activated during walking.

https://doi.org/10.1038/s41592-024-02583-1

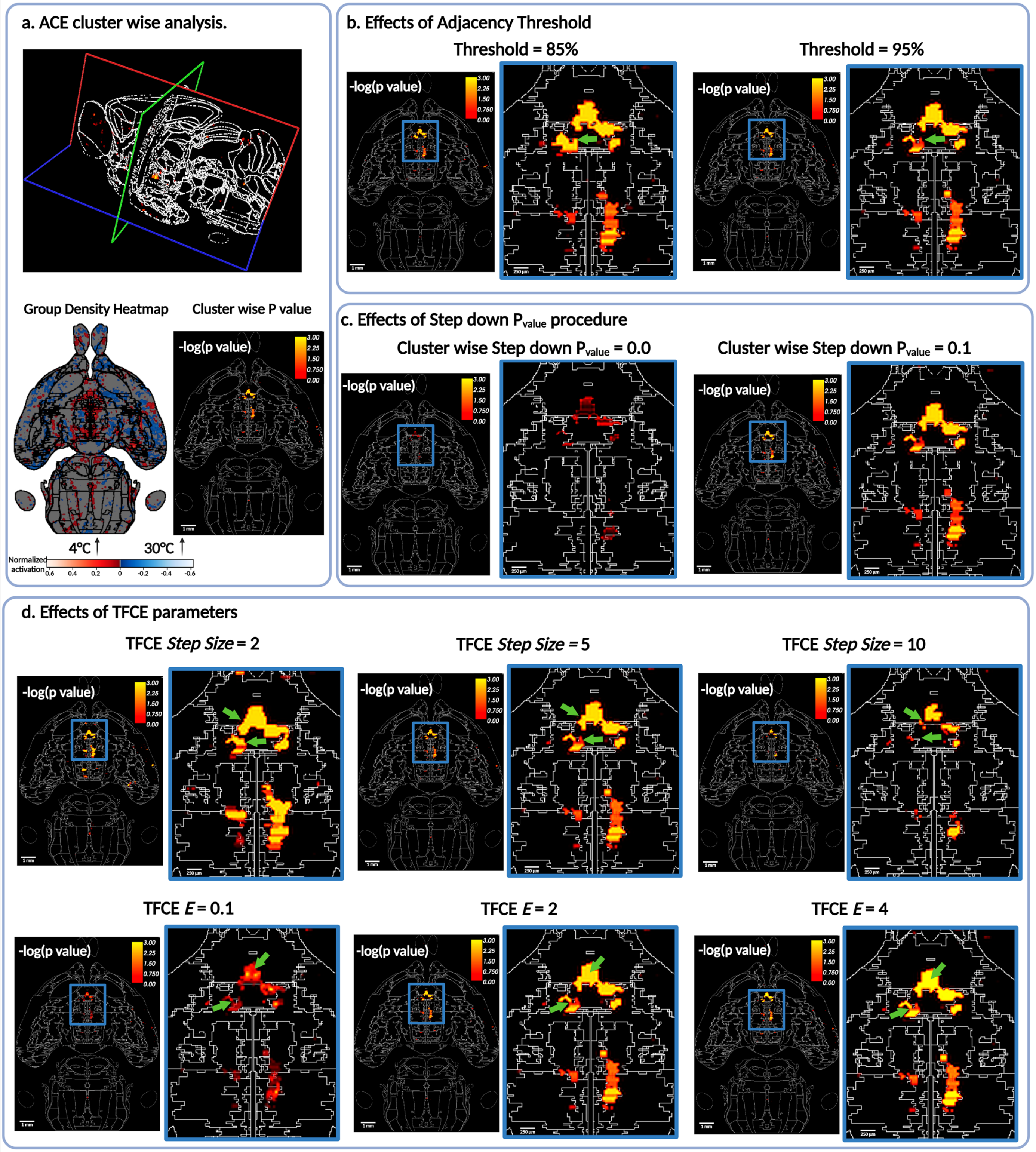

Extended Data Fig. 10 | The effects of different user-fed parameters to control the rigor of ACE cluster-wise statistics. a. An axial view of the group density heatmap next to its corresponding ACE cluster-wise p-value map for the cold-induced experiment. **b-d**. The effects of the threshold used to define the adjacency matrix (**b**), Step-down p-value (**c**), TFCE step size, and TFCE *E* (**d**) on the results of ACE cluster-wise TFCE permutation algorithm. See Methods - Cluster-wise permutation-based statistical algorithm and analysis for more details.

nature portfolio

Corresponding author(s): Maged Goubran

Last updated by author(s): Oct 2, 2024

Reporting Summary

Nature Portfolio wishes to improve the reproducibility of the work that we publish. This form provides structure for consistency and transparency in reporting. For further information on Nature Portfolio policies, see our Editorial Policies and the Editorial Policy Checklist.

Statistics

For all statistical analyses, confirm that the following items are present in the figure legend, table legend, main text, or Methods section.

n/a	Confirmed	
□	☒	The exact sample size (*n*) for each experimental group/condition, given as a discrete number and unit of measurement
□	☒	A statement on whether measurements were taken from distinct samples or whether the same sample was measured repeatedly
□	☒	The statistical test(s) used AND whether they are one- or two-sided *Only common tests should be described solely by name; describe more complex techniques in the Methods section.*
□	☒	A description of all covariates tested
□	☒	A description of any assumptions or corrections, such as tests of normality and adjustment for multiple comparisons
□	☒	A full description of the statistical parameters including central tendency (e.g. means) or other basic estimates (e.g. regression coefficient) AND variation (e.g. standard deviation) or associated estimates of uncertainty (e.g. confidence intervals)
□	☒	For null hypothesis testing, the test statistic (e.g. *F*, *t*, *r*) with confidence intervals, effect sizes, degrees of freedom and *P* value noted *Give P values as exact values whenever suitable.*
☒	□	For Bayesian analysis, information on the choice of priors and Markov chain Monte Carlo settings
□	☒	For hierarchical and complex designs, identification of the appropriate level for tests and full reporting of outcomes
□	☒	Estimates of effect sizes (e.g. Cohen's *d*, Pearson's *r*), indicating how they were calculated

Our web collection on statistics for biologists contains articles on many of the points above.

Software and code

Policy information about availability of computer code

Data collection	For unseen dataset 1 and walking experiment datasets, tissue clearing was done using a custom-made protocol based iDISCO+ and for training, unseen dataset 2, and cold-induced experiment datasets, it was done using SHIELD protocols with LifeCanvas Technologies through contracted service. Imaging of tissue in 3D was performed on a CLARITY-optimized light sheet microscope for the unseen and walking experiment datasets and LifeCanvas Technologies SmartSPIM microscope.
Data analysis	The ACE code uses Python 3.7.3, Pytorch v1.13.1, MONAI v0.9.dev2202, Numpy v1.18.5, Scipy v1.7.3, and mne package v1.3.1 in addition to ImageJ/Fiji macros (https://imagej.net/ software/fiji/). For registration and ROI-based analysis we used MIRACL (https://miracl.readthedocs.io/). The ACE performance was compared against Ilastik-1.4.0rc8 (https://www.ilastik.org/) and Cellfinder v0.4.21 (https://github.com/brainglobe/cellfinder). The figures in the paper were made using matplotlib v3.4.3, seaborn v0.12.2, ITK-SNAP v3.8.0 (http://www.itksnap.org/pmwiki/pmwiki.php), Napari v0.4.17, ImageJ/Fiji, FreeSurfuer freeview package v6 (https://surfer.nmr.mgh.harvard.edu/), and brainrender package v2.0.5.5 (https://github.com/brainglobe/brainrender).

For manuscripts utilizing custom algorithms or software that are central to the research but not yet described in published literature, software must be made available to editors and reviewers. We strongly encourage code deposition in a community repository (e.g. GitHub). See the Nature Portfolio guidelines for submitting code & software for further information.

Data

Policy information about availability of data

All manuscripts must include a data availability statement. This statement should provide the following information, where applicable:

- Accession codes, unique identifiers, or web links for publicly available datasets
- A description of any restrictions on data availability
- For clinical datasets or third party data, please ensure that the statement adheres to our policy

A subset of the datasets (a whole-brain LSFM data and the voxelized and warped segmentation maps) generated and analyzed during the current study is available at www.miracl.readthedocs.io/ under ACE workflow tutorial as examples with the pipeline. All the required files such as Allen atlas and labels and datasets are included in the Docker container of MIRACL with documentation and tutorials.

Research involving human participants, their data, or biological material

Policy information about studies with human participants or human data. See also policy information about sex, gender (identity/presentation), and sexual orientation and race, ethnicity and racism.

Reporting on sex and gender	N/A
Reporting on race, ethnicity, or other socially relevant groupings	N/A
Population characteristics	N/A
Recruitment	N/A
Ethics oversight	N/A

Note that full information on the approval of the study protocol must also be provided in the manuscript.

Field-specific reporting

Please select the one below that is the best fit for your research. If you are not sure, read the appropriate sections before making your selection.

☒ Life sciences ☐ Behavioural & social sciences ☐ Ecological, evolutionary & environmental sciences

For a reference copy of the document with all sections, see nature.com/documents/nr-reporting-summary-flat.pdf

Life sciences study design

All studies must disclose on these points even when the disclosure is negative.

Sample size	Group size was not pre-determined based on statistical power law but is based on previously published studies (Lal, N. K. et al. Xiphoid nucleus of the midline thalamus controls cold-induced food seeking. Nature 621, 138–145 (2023).)
Data exclusions	No data was excluded from the study.
Replication	We successfully tested against state-of-the-art algorithms using five whole brain LSFM data and four completely out-of-distribution whole brain LSFM data.
Randomization	For the walking and cold experiments, animals of the same age, sex, and weight were randomly into treatment or control groups.
Blinding	All annotators worked in isolation and were blind to specific groups.

Reporting for specific materials, systems and methods

We require information from authors about some types of materials, experimental systems and methods used in many studies. Here, indicate whether each material, system or method listed is relevant to your study. If you are not sure if a list item applies to your research, read the appropriate section before selecting a response.

Materials & experimental systems

n/a	Involved in the study
☐	☒ Antibodies
☒	☐ Eukaryotic cell lines
☒	☐ Palaeontology and archaeology
☐	☒ Animals and other organisms
☒	☐ Clinical data
☒	☐ Dual use research of concern
☒	☐ Plants

Methods

n/a	Involved in the study
☒	☐ ChIP-seq
☒	☐ Flow cytometry
☒	☐ MRI-based neuroimaging

Antibodies

Antibodies used

Primary antibodies:
For cold and unseen dataset 2; c-Fos (9F6) Rabbit mAb (Cell Signaling, #2250S); for more details refer to https://doi.org/10.1038/s41586-023-06430-9
For unseen dataset 1 and walking datasets; c-Fos (rabbit anti-cFos, 1:2000, Synaptic Systems, #226 003)

Secondary antibodies:
For cold and unseen dataset 2; Alexa Fluor® 488 Anti-Rabbit IgG (Jackson ImmunoResearch, #711-546-152); for more details refer to https:// doi.org/10.1038/s41586-023-06430-9
For unseen dataset 1 and walking datasets; Alexa Fluor® 647 donkey anti-rabbit IgG (Thermo Fisher Scientific, #A-31573)

Validation

The use and validation of these antibodies have been established in previous studies that can be referred on the manufactures websites below:

Primary antibody:
Cold and unseen dataset 1: https://www.cellsignal.com/products/primary-antibodies/c-fos-9f6-rabbit-mab/2250
Unseen dataset 2and walking datasets: https://sysy.com/product/226003

Secondary antibody:
Cold and unseen dataset 2: https://www.jacksonimmuno.com/catalog/products/711-546-152
Unseen dataset 1 and walking datasets: https://www.thermofisher.com/antibody/product/Donkey-anti-Rabbit-IgG-H-L-Highly-Cross-Adsorbed- Secondary-Antibody-Polyclonal/A-31573

Animals and other research organisms

Policy information about studies involving animals; ARRIVE guidelines recommended for reporting animal research, and Sex and Gender in Research

Laboratory animals

For the training dataset, TRAP2-Ai9 mice (Mus Musculus) strain was used (n=10, 3-4 months old, n=8, 2 months old). All were obtained from the Scripps Research Department of Animal Resources rodent breeding colony.
For the unseen dataset 1, C57BL/6 mice strain was used (n=3, female, ~8 weeks old).
For the cold dataset, C57BL/6 mice strain was used (n=4 / group, and male), were obtained from the Scripps Research Department of Animal Resources rodent breeding colony; more details refer to https://doi.org/10.1038/s41586-023-06430-9
For the walking dataset, C57BL/6 mice strain was used. These mice, n=6 (~8 weeks age, female).
For unseen dataset 2, a male C57BL/6J mouse (Jackson Laboratory, strain 000664), aged 18 months old.

Wild animals

The study did not involve wild animals.

Reporting on sex

Training dataset was contained both male and female mice.
Cold experiment was done using only male mice; for more details refer to https://doi.org/10.1038/s41586-023-06430-9 Walking experiment was done using only female mice.

Field-collected samples

Study did not involve sample collected from the field.

Ethics oversight

Training dataset experiments: All animal procedures followed animal care guidelines
approved by the Institution Animal Care and Use Committee at the Scripps Research Institute.
Unseen dataset 1 experiments: All procedures were performed in compliance with the Swiss Veterinary Law guidelines and approved by the Veterinary Office of the Canton of Geneva (Switzerland; license GE/112/20).
Cold dataset experiments: Experiments were approved by the Scripps Research Institute's or BIDMC's Institutional Animal Care and Use Committee (IACUC), respectively. All experiments were under the guidelines of the NIH; for more details refer to https://doi.org/10.1038/s41586-023-06430-9
Walking dataset experiment: All procedures were performed in compliance with the Swiss Veterinary Law guidelines and approved by the Veterinary Office of the Canton of Geneva (Switzerland; license GE/112/20).

Unseen dataset 2 experiments: All animal procedures followed protocols approved by the Stanford University Institutional Animal Care and Use Committee, and met the guidelines of the National Institutes of Health Guide for the Care and Use of Laboratory Animals.

Note that full information on the approval of the study protocol must also be provided in the manuscript.

Plants

Seed stocks

Report on the source of all seed stocks or other plant material used. If applicable, state the seed stock centre and catalogue number. If plant specimens were collected from the field, describe the collection location, date and sampling procedures.

Novel plant genotypes

Describe the methods by which all novel plant genotypes were produced. This includes those generated by transgenic approaches, gene editing, chemical/radiation-based mutagenesis and hybridization. For transgenic lines, describe the transformation method, the number of independent lines analyzed and the generation upon which experiments were performed. For gene-edited lines, describe the editor used, the endogenous sequence targeted for editing, the targeting guide RNA sequence (if applicable) and how the editor was applied.

Authentication

Describe any authentication procedures for each seed stock used or novel genotype generated. Describe any experiments used to assess the effect of a mutation and, where applicable, how potential secondary effects (e.g. second site T-DNA insertions, mosiacism, off-target gene editing) were examined.